J. Fluid Mech. (2019), *vol.* 880, *pp.* 992–1019.
doi:10.1017/jfm.2019.726

Drag forces on sparsely packed cube arrays

X. I. A. Yang[1], H. H. A. Xu[1], X. L. D. Huang[1] and M.-W. Ge[2,†]

[1]Mechanical Engineering, Penn State University, State College, PA 16802, USA

[2]State Key Laboratory of Alternate Electrical Power System with Renewable Energy Sources, North China Electric Power University, Beijing 102206, PR China

(Received 16 January 2019; revised 25 August 2019; accepted 26 August 2019; first published online 18 October 2019)

Flow over aligned and staggered cube arrays is a classic model problem for rough-wall turbulent boundary layers. Earlier studies of this model problem mainly looked at rough surfaces with a moderate coverage density, i.e. $\lambda_p > O(3\,\%)$, where λ_p is the surface coverage density and is defined to be the ratio between the area occupied by the roughness and the total ground area. At lower surface coverage densities, i.e. $\lambda_p < O(3\,\%)$, it is conventionally thought that cubical roughness acts like isolated roughness elements; and that the single-cube drag coefficient, i.e. $C_d \equiv f/(\rho U_h^2 h^2)$, equals C_R. Here, f is the drag force on one cubical roughness element, $\rho = \text{const.}$ is the fluid density, h is the height of the cube, U_h is the spatially and temporally averaged wind speed at the cube height, and C_R is the drag coefficient of an isolated cube. In this work, we conduct large-eddy simulations and direct numerical simulations of flow over wall-mounted cubes with very low surface coverage densities, i.e. $0.08\,\% < \lambda_p < 4.4\,\%$. The large-eddy simulations are at nominally infinite Reynolds numbers. The results challenge the conventional thinking, and we show that, at very low surface coverage densities, the single-cube drag coefficient may increase as a function of λ_p. Our analysis suggests that this behaviour may be attributed to secondary turbulent flows. Secondary turbulent flows are often found above spanwise-heterogeneous roughness. Although the roughness considered in this work is nominally homogeneous, the secondary flows in our simulations are very similar to those observed above spanwise-heterogeneous surface roughness. These secondary vortices redistribute the fluid momentum in the outer layer, leading to high-momentum pathways above the wall-mounted cubes and low-momentum pathways at the two sides of the wall-mounted cubes. As a result, the spatially and temporally averaged wind speed at the cube height, i.e. U_h, is an underestimate of the incoming flow to the cubes, which in turn leads to a large drag coefficient C_d.

Key words: turbulence simulation, turbulence modelling

1. Introduction

Rough-wall turbulent boundary layers are encountered in both nature and engineering (Raupach, Antonia & Rajagopalan 1991; Barlow & Coceal 2008; Bons 2010). Modelling drag forces on rough walls is a research topic that has received sustained

† Email address for correspondence: gemingwei@ncepu.edu.cn

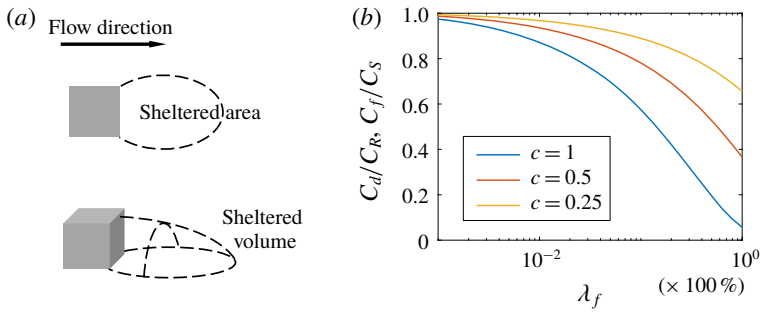

FIGURE 1. (Colour online) (*a*) Sketches of the sheltered ground area and the sheltered volume downstream of a cubical roughness element: top view (upper part) and perspective view (lower part). (*b*) The drag and friction coefficients computed according to (1.3) and (1.4) for $c_1 = c_2 = c = 0.25,\ 0.5$ and 1.

attention (Jiménez 2004; Schultz & Flack 2009; Schlichting & Gersten 2016). Recently, with increasing use of additive manufactured parts in the turbomachinery industry, a new interest has emerged in modelling drag forces on 3D printed rough surfaces (see e.g. Ferster, Kirsch & Thole 2018; Kirsch & Thole 2018).

A well-studied model problem for rough-wall turbulent boundary layers is flow over aligned and staggered cube arrays (see e.g. Coceal *et al.* 2006; Cheng *et al.* 2007; Leonardi & Castro 2010; Lee, Sung & Krogstad 2011). Aside from empirical models (Moody 1947; Taylor, Coleman & Hodge 1985), the theoretical work by Arya (1975) and Raupach (1992) on drag partition lays the groundwork of rough-wall drag-force modelling. Raupach argues that a cubical roughness element 'shelters' its downstream ground area and volume (see figure 1*a*). The sheltered ground area and the sheltered volume scale as h^2U_h/u_τ and h^3U_h/u_τ, respectively, where h is the cube height, U_h is the spatially and temporally averaged wind speed at the cube height, and u_τ is the friction velocity. If a roughness element is not sheltered, it acts as an isolated element. Raupach (1992) concludes that, at low surface coverage densities, the drag force on a rough surface increases linearly with the number of roughness elements (given an outer flow), and the single-cube drag coefficient,

$$C_d \equiv f/(\rho U_h^2 h^2), \tag{1.1}$$

equals that of an isolated element. Here, $\rho = \text{const.}$ is the fluid density and f is the drag force on one wall-mounted cube. For cubes, the solidity λ_f equals the surface coverage density λ_p. Sheltering becomes non-negligible for surfaces with a moderate coverage density. Raupach (1992) hypothesizes that the overall shelter area and volume can be calculated by randomly superimposing the individual shelter areas and volumes. He concludes that the surface friction drag force scales as $\tau_s(\lambda_p) = \rho C_s U_h^2 \exp(-c_1\lambda_p U_h/u_\tau)$ and that the roughness-induced drag scales as $\tau_R(\lambda_p) = \lambda_p \rho C_R U_h^2 \exp(-c_2\lambda_p U_h/u_\tau)$, where τ_s and τ_R are the surface drag and the roughness drag per unit planar area, C_s and C_R are the friction coefficient of the unmounted ground and the drag coefficient of an isolated cube, respectively, and c_1 and c_2 are two $O(1)$ constants, whose values depend on the roughness arrangement. Because τ_s and τ_R are partitions of the total drag force, the above theory is conventionally referred to as the drag partition theory.

We define the friction coefficient as

$$C_f = \tau_s/(\rho U_h^2). \tag{1.2}$$

A direct consequence of the drag partition theory is that

$$C_f(\lambda_p) \equiv \frac{\tau_s}{\rho U_h^2} = C_s \exp(-c_1 \lambda_p U_h/u_\tau) \leqslant C_s \tag{1.3}$$

and

$$C_d(\lambda_p) \equiv \frac{f}{\rho U_h^2 h^2} = \frac{\tau_R}{\lambda_p \rho U_h^2} = C_R \exp(-c_2 \lambda_p U_h/u_\tau) \leqslant C_R. \tag{1.4}$$

Defining $\gamma = U_h/u_\tau$, the drag partition $\tau = \rho u_\tau^2 = \tau_s + \tau_R$ leads to

$$C_s \gamma^2 \exp(-c_1 \lambda_p \gamma) + \lambda_p C_R \gamma^2 \exp(-c_2 \lambda_p \gamma) = 1. \tag{1.5}$$

Solving (1.5) for γ, substituting the solution into (1.3) and (1.4), and setting $c_1 = c_2 = c$, $C_R = 0.5$ and $C_s = 0.001$, i.e. typical values in the literature (ESDU 1986; Raupach 1992), figure 1(*b*) shows C_f/C_s and C_d/C_R as a function of λ_p. Because $c_1 = c_2$, we have $C_f/C_s = C_d/C_R$. The result shows that, given c, both C_f/C_s and C_d/C_R are non-increasing functions of the surface coverage density, λ_p.

The pioneering work by Raupach (1992) on drag partition and flow sheltering lays the groundwork for later studies on rough-wall drag-force modelling (see e.g. Shao & Yang (2005, 2008)). Determining the drag partition is often the most important part of a rough-wall model. Here, a rough-wall model refers to a model that predicts the mean flow in a rough-wall boundary layer and is also referred to as a canopy model. Examples of such models include the ones presented in Macdonald (2000), Coceal & Belcher (2004) and Harman & Finnigan (2007), to name a few, where the parametrization of flow sheltering relies on empiricism, and the ones presented in Millward-Hopkins *et al.* (2011) and Yang *et al.* (2016), where sheltering is modelled, and the authors were able to predict the aerodynamic properties of arbitrary cube-roughened surfaces (see e.g. Yang (2016) and Yang & Meneveau (2016, 2017)). Because sheltering leads to reduced friction and pressure drag, it is a defining feature of rough-wall models that both C_d and C_f are non-increasing functions of the surface coverage density.

In this work, we revisit the classic drag partition theory. We study drag forces on sparsely packed cubes with an aligned or a staggered arrangement. Aligned and staggered cubes are well studied. Direct numerical simulation (DNS) results of a fully developed channel with wall-mounted cubes were reported in, for example, Coceal *et al.* (2006), Coceal *et al.* (2007*b*) and Leonardi & Castro (2010). Large-eddy simulations (LES) were conducted by Stoesser *et al.* (2003), Castillo, Inagaki & Kanda (2011), Inagaki *et al.* (2012) and Cheng & Porté-Agel (2015), to name a few. Finally, Cheng & Castro (2002), Cheng *et al.* (2007) and Perret *et al.* (2017) reported experimental measurements of drag forces on cubical roughness. The previous studies provided data for surfaces with a coverage density from approximately 3 % to approximately 40 %. Depending on the amount of flow sheltering, roughness may be categorized into *k*-type and *d*-type (Perry, Schofield & Joubert 1969; Jiménez 2004): *k*-type roughness has limited sheltering, and the roughness elements act similarly to isolated elements; *d*-type roughness has a lot of sheltering, and the flow does not experience much drag from each roughness element.

In this work, we study cubical roughness. But different from previous studies that considered surfaces with a moderate coverage density, we study drag forces on sparsely packed cubes. The objective of this work is to test if the classic view of Raupach (1992) holds at very low surface coverage densities, and, if not, what might be causing the deviation. To do that, we conduct LES of flow over aligned and staggered cube arrays with surface coverage densities between 0.08 % and 4.4 %. We show that, for both aligned and staggered arrangements, within a certain range of surface coverage densities, the single-cube drag coefficient C_d is an increasing function of λ_p. In addition to LES, we conduct DNS of aligned cubes at one surface coverage density, $\lambda_p = 1\,\%$. We use the DNS to study the behaviour of skin friction. The rest of the paper is organized as follows. The detailed computational set-up is described in § 2. We study the behaviour of drag forces in § 3. A brief discussion about the secondary flows is presented in § 4. Concluding remarks are given in § 5. In appendices A and B, we validate our results by comparing with wind tunnel experiments and wall-resolved LES.

Rough-wall boundary layer flow is a classic problem and may be approached from many perspectives. The discussion here will focus on low-order flow quantities. Throughout the paper, we use u (U), v (V) and w (W) for the streamwise, spanwise and wall-normal velocities. We use capital letters, U, V and W, for time-averaged flow quantities. When necessary, we also use $\langle\cdot\rangle$ to indicate time averaging. Subscripts x and y are used to denote spatial averaging in the streamwise and spanwise directions, respectively. For example, U_x is the streamwise-averaged and time-averaged streamwise velocity, and U_{xy} is the horizontally averaged and time-averaged streamwise velocity. Lower-case letters, u, v and w, are used for instantaneous flow quantities.

2. Computation details

2.1. *Large-eddy simulations*

We use LES for flow over sparsely packed cubes in a half-channel. LES resolves the relatively energetic motions and models the relatively less energetic motions and is therefore a very cost-effective computational tool (Meneveau & Katz 2000). The LES code we use is LESGO. It solves the filtered incompressible Navier–Stokes equations at nominally infinite Reynolds number. The convective terms are evaluated in its rotational form. A pseudo-spectral discretization is used in both the streamwise and spanwise directions. A second-order finite difference scheme is used in the wall-normal direction. Conserved flow quantities, including the streamwise, wall-normal and spanwise velocities, are solved on a staggered grid (as opposed to a collocated one). The wall-mounted cubes are resolved using an immersed boundary method. The cube surfaces are such that they coincide with the surfaces of the pressure computational cells. The deviatoric part of the subgrid-scale stress is modelled via the scale-dependent Lagrangian dynamic model (Bou-Zeid, Meneveau & Parlange 2005). The code has been extensively used for similar flow problems (see e.g. Cheng & Porté-Agel (2015), Yang *et al.* (2016) and Giometto *et al.* (2017)). The reader is directed to Yang & Abkar (2018) for further details of the solver.

Figure 2 shows the computational domain. The height of the wall-mounted cubes is h. The domain size is $L_x \times L_y \times L_z$ in the streamwise, spanwise and wall-normal directions, respectively. The half-channel height is $L_z = 3.5h$ for all the cases except for A100-h, where the half-channel height is $L_z = 7h$. The flow is driven by a constant

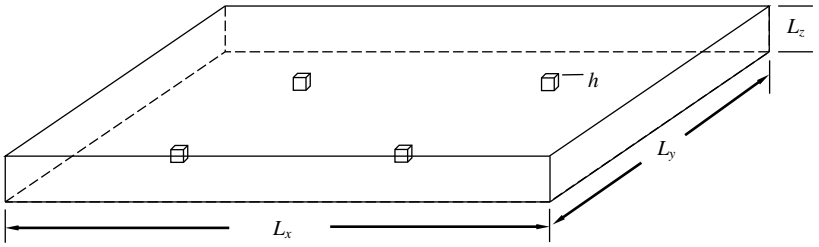

FIGURE 2. A sketch of the computational domain. Periodicity is imposed in both the streamwise (x) and spanwise (y) directions. The cubes are of height h. The size of the computational domain is $L_x \times L_y \times L_z$.

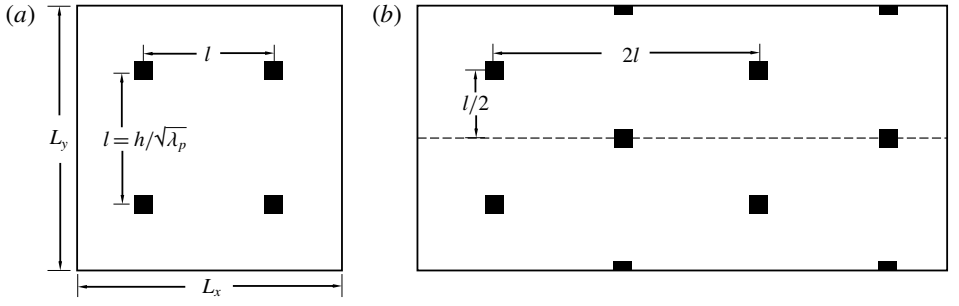

FIGURE 3. Sketches of the two roughness arrangements: (a) aligned arrangement and (b) staggered arrangement. The flow goes from left to right.

volumetric body force f_b. The friction velocity is $u_\tau = \sqrt{f_b L_z/\rho}$ and is kept constant. We vary L_x and L_y. The streamwise and spanwise extents of the computational domain are such that they are never smaller than approximately $2\pi L_z$. According to Lozano-Durán & Jiménez (2014), our computational domain is sufficiently large. It is worth noting that domains that are much smaller were used to study rough-wall boundary layer flows at moderate surface coverage densities (Chung *et al.* 2015; MacDonald *et al.* 2016, 2017).

Table 1 summarizes all the LES cases. By varying L_x, L_z and the number of wall-mounted cubes in the computational domain, we consider rough walls with surface coverage densities between 0.081 % and 4.4 %. Two extensively studied roughness arrangements are considered, namely, the aligned and the staggered arrangements. Figure 3(a,b) shows the sketches of the two arrangements. For an aligned cube array, both the streamwise and the spanwise inter-cube distances are $l = h/\sqrt{\lambda_p}$, which varies from approximately $4h$ to $35h$. The streamwise distance between two cubes is $2l$ when the cubes are staggered in the spanwise direction. If we project the wall-mounted cubes onto a spanwise–wall-normal plane, for a staggered arrangement, the spanwise distance between two neighbouring cubes is $l/2$.

The boundary conditions are as follows. A periodic boundary condition is imposed in both the streamwise and spanwise directions for all cases except for A100-d and A440-d, where the inflow is provided by a precursor channel flow simulation. A free-slip condition is used for the top boundary. The surface shear stresses on both the

Name	λ_p (%)	$L_x \times L_y \times L_z$	Mesh	N	Name	λ_p (%)	$L_x \times L_y \times L_z$	Mesh	N
A008	0.081	$70 \times 70 \times 3.5$	9.1M	2×2	S008	0.081	$70 \times 70 \times 3.5$	9.1M	2×2
A011	0.11	$60 \times 60 \times 3.5$	6.7M	2×2	S011	0.11	$60 \times 60 \times 3.5$	6.7M	2×2
A016	0.16	$50 \times 50 \times 3.5$	4.6M	2×2	S016	0.16	$50 \times 50 \times 3.5$	4.6M	2×2
A025	0.25	$40 \times 40 \times 3.5$	3.0M	2×2	S025	0.25	$40 \times 40 \times 3.5$	3.0M	2×2
A044	0.44	$30 \times 30 \times 3.5$	1.7M	2×2	S044	0.44	$30 \times 30 \times 3.5$	1.7M	2×2
A100	1.0	$20 \times 20 \times 3.5$	0.74M	2×2	S100	1.0	$20 \times 20 \times 3.5$	0.74M	2×2
A150	1.5	$25 \times 25 \times 3.5$	1.1M	3×3	S150	1.5	$33 \times 25 \times 3.5$	1.1M	4×3
A300	3.0	$23 \times 23 \times 3.5$	0.98M	4×4	S360	3.6	$21 \times 21 \times 3.5$	0.82M	4×4
A440	4.4	$24 \times 24 \times 3.5$	1.0M	5×5	S440	4.4	$29 \times 24 \times 3.5$	1.3M	6×5
A100-h	1.0	$40 \times 40 \times 7.0$	5.8M	4×4					
A100-w	1.0	$40 \times 40 \times 3.5$	3.0M	4×4					
A100-d	1.0	$100 \times 20 \times 3.5$	3.6M	8×2					
A440-d	4.4	$95 \times 24 \times 3.5$	4.0M	16×5					

TABLE 1. LES cases. The names of cases are Axxx or Sxxx, where 'A' and 'S' denote 'aligned' and 'staggered' arrangements, respectively, and the three digits 'xxx' indicate the surface coverage density. Case A100-h is similar to A100 but in a horizontally larger and vertically higher computational domain, i.e. $L_x \times L_y \times L_z = 40 \times 40 \times 7$. Case A100-w is similar to A100 but in a horizontally larger computational domain, i.e. $L_x \times L_y \times L_z = 40 \times 40 \times 3.5$. Cases A100-d and A440-d are similar to A100 and A440 but with the inflows specified using a precursor channel flow simulation. The domain sizes are shown in terms of the cube height h. The 'Mesh' column shows the grid size in million (M) cells. The column 'N' shows the number of wall-mounted cubes in columns (streamwise) and rows (spanwise). Note that we keep two significant digits for all the numbers.

ground and the cube surfaces are specified through a wall model,

$$\boldsymbol{\tau}/\rho = -\left[\frac{\kappa}{\log(\Delta/z_o)}\right]^2 \tilde{\boldsymbol{U}}_{\parallel}|\tilde{\boldsymbol{U}}_{\parallel}|, \tag{2.1}$$

where $\boldsymbol{\tau}$ is the shear stress vector, $\boldsymbol{U}_{\parallel}$ is the wall-parallel velocity vector at a distance Δ from the wall, $\tilde{\cdot}$ is a spatial filtering operator (Bou-Zeid *et al.* 2005; Yang, Park & Moin 2017*b*), $z_o = 10^{-4}h$ is a pre-specified roughness/viscous length scale, $\kappa = 0.4$ is the von Kármán constant (von Kármán 1931; Marusic *et al.* 2013) and log is the natural logarithm. Equilibrium wall models including the one in (2.1) have difficulties in handling flow separations and predicting flow reattachments (Slotnick *et al.* 2014). This is less of an issue for sparsely packed roughness. For a cubical roughness element, the flow separates at the trailing edge irrespective of the wall model used. Also, because we study cube arrays that are very sparsely packed, the flow reattaches before the recirculation bubble reaches the downstream wall-mounted cube, which is clear from figure 4, where we show contours of the mean streamwise velocities on a streamwise–wall-normal plane through the centre of a column of wall-mounted cubes. In figure 4, two neighbouring cubes are $4.8h$ apart in the streamwise direction, which is the closest among the cases in table 1. Hence, it is probably safe to say that, at very low surface coverage densities, the drag forces on the wall-mounted cubes do not depend critically on near-wall modelling.

For all cases in table 1, we use a uniform grid, with $\Delta x = \Delta y = \Delta z = h/8$. The same grid resolution has previously been used in a number of studies (Xie & Castro 2006; Jiang *et al.* 2008; Graham & Meneveau 2012). The results are also validated

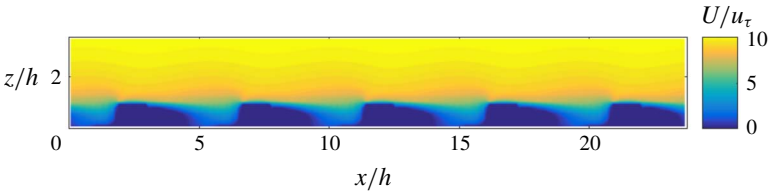

FIGURE 4. (Colour online) Contours of the mean streamwise velocity on a streamwise–wall-normal plane through the centre of a column of wall-mounted cubes. We show results from A440. The contour levels cut off at $U=0$ to highlight the reattachment location. The flow reattached before the recirculation bubble reaches the next cube.

by comparing with wind tunnel measurements and wall-resolved LES in appendices A and B.

2.2. *Direct numerical simulation*

The near-wall turbulence is modelled instead of resolved in LES. To get more reliable measurements at the wall and to study the behaviour of the skin friction, we resort to DNS. The computational set-up is the same as in the case A100. We refer to the DNS as A100-d. A structured, body-fitted mesh is used. The size of the mesh is approximately 9.6 million. We refine the mesh near the wall-mounted cubes. Figure 5(*a*,*b*) shows the mesh near a wall-mounted cube. The grid resolution is such that the local wall-normal resolution is nowhere coarser than $\Delta_n^+ = 0.5$ and the local wall-parallel resolution is $\Delta_\parallel^+ \approx 5$. Compared with resolutions used for similar flow problems (Coceal, Dobre & Thomas 2007*a*; Balakumar, Park & Pierce 2014), our grid resolution is quite high. Similar to A100, the flow is driven by a constant body force. The friction Reynolds number is $Re_\tau = u_\tau L_z/\nu = 350$. Case A100 is at a nominally infinite Reynolds number. Considering the difference in their Reynolds numbers, the drag and the friction in A100 and A100-d are not expected to be the same, although the LES and the DNS solutions are qualitatively alike. For the DNS, we use the in-house unstructured finite-volume flow solver CharLES (Khalighi *et al.* 2011; Bermejo-Moreno *et al.* 2014). The code solves the full compressible Navier–Stokes equation. It uses a fourth-order-accurate spatial discretization (Mahesh, Constantinescu & Moin 2004) and a third-order-accurate temporal discretization (Williamson 1980; Moin 2010). The Mach number in the computational domain is nowhere greater than 0.15, and therefore the flow may be considered as incompressible (Lele 1994; Park & Moin 2014). The code is well validated and has been used extensively for boundary layer flow problems (Joo *et al.* 2014; Larsson *et al.* 2015; Park 2017).

3. Drag forces and flow physics

It is the conclusion of the classic drag partition theory that C_d ($< C_R$) is a non-increasing function of λ_p. This is often the starting point of rough-wall drag-force modelling. Here, we show results that challenge the above classic theory. Figure 6(*a*) shows the drag coefficient C_d as a function of the surface coverage density λ_p for both the aligned and the staggered arrays. For the staggered arrays, the drag coefficient C_d is approximately 0.49 and stays roughly constant for $\lambda_p < 0.25\,\%$. It increases as a function of λ_p from $\lambda_p = 0.25\,\%$ to $\lambda_p \approx 5\,\%$. For the aligned arrays, the drag coefficient increases as a function of λ_p from $\lambda_p = 0.08\,\%$ to approximately $\lambda_p = 1\,\%$,

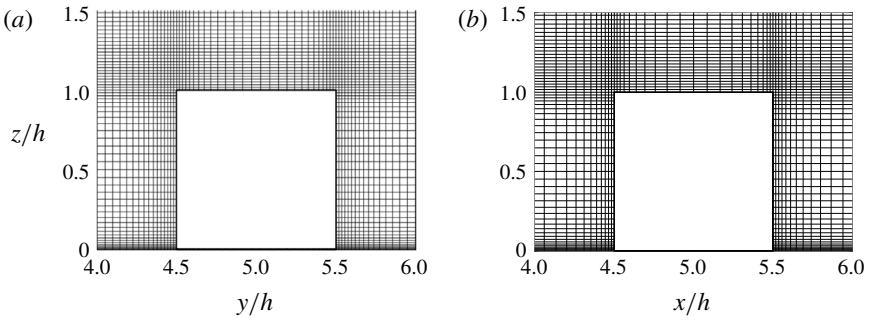

FIGURE 5. Grid near a wall-mounted cube: (*a*) on a spanwise–wall-normal plane and (*b*) on a streamwise–wall-normal plane.

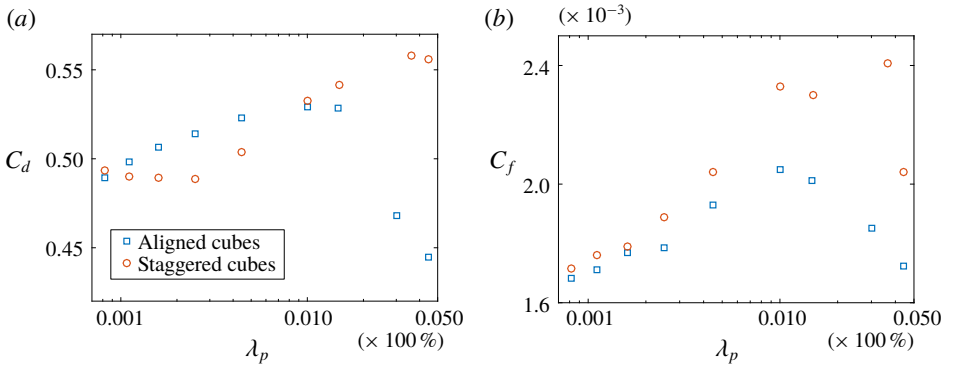

FIGURE 6. (Colour online) (*a*) Drag coefficient $C_d = f/(\rho U_h^2 h^2)$ as a function of the surface coverage density λ_p for both the aligned and the staggered cube arrays. Here, f is the drag force on one wall-mounted cube; and U_h is the mean velocity at the cube height. The red circles show the results of the staggered cube arrays, and the blue squares show the results of the aligned cube arrays. (*b*) Friction coefficient $C_f = \tau_s/(\rho U_h^2)$ as a function of the surface coverage density λ_p. Here, τ_s is the friction drag per unit planar area. The symbols are the same as in panel (*a*).

and then decreases as a function of λ_p for $\lambda_p > 1.5\,\%$. Figure 6(*b*) shows the friction coefficient C_f as a function of the surface coverage density. For both arrangements, the skin-friction coefficient increases as a function of λ_p for $\lambda_p < 1\,\%$. Note that C_d is the drag coefficient of a single cube, not the skin-friction coefficient of the entire rough wall, the latter of which is an increasing function of the surface coverage density until approximately $\lambda_p \approx 15\,\%$–$30\,\%$ (Jiménez 2004).

There are a few trends that are expected from the classic drag partition theory and a number of trends that are less expected. First, we briefly discuss the trends that are expected from the theory. The decrease of the drag coefficient and the friction coefficient as a function of λ_p at relatively high coverage densities (although only a few per cent) is expected and is simply a result of flow sheltering (Yang *et al.* 2016). For the staggered cubes, at very low surface coverage densities, i.e. $\lambda_p < 0.25\,\%$, the cubes act as isolated elements, and the drag coefficient stays constant, $C_d = C_R = 0.49$. The drag coefficient $C_R = 0.49$ is close to the measurements in the literature, although the exact value may vary depending on the flow conditions, including the Reynolds

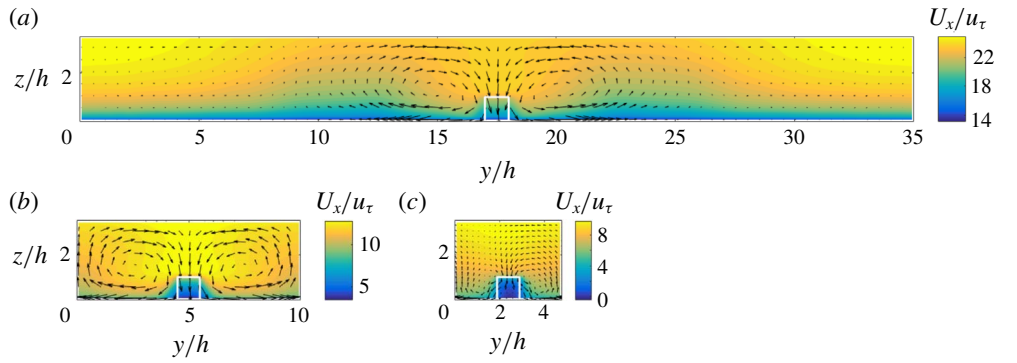

FIGURE 7. (Colour online) Contours of the streamwise velocity: results for aligned cases (*a*) A008, (*b*) A100 and (*c*) A440. The vectors show the in-plane motions (spanwise and wall-normal velocities). Both the spanwise and the wall-normal velocities are averaged in time and in the streamwise direction. The vectors are shown every four grid points in both directions in (*a*,*b*), and every other point in (*c*) for better presentation. The cubes are projected onto the plane. The flow is periodic in the spanwise direction. We show only one repeating flow unit.

number and the boundary layer height (Akins, Peterka & Cermak 1977; ESDU 1986; Macdonald, Griffiths & Hall 1998). Last (and needless to say) the flow behaves differently above aligned and staggered cubes. Next, we discuss the trends that are not expected from the drag partition theory, i.e. the increase of the drag coefficient and the skin-friction coefficient as a function of the surface coverage density. Flow sheltering leads to reduced drag forces and cannot be responsible for a drag coefficient larger than C_R. Here, the increase of the drag coefficient as a function of λ_p is a result of secondary turbulent flows. Secondary flows are common in, for example, square ducts and open channels (Nikuradse 1930; Nakagawa 2017). In the context of canonical boundary layer flows, secondary flows arise often as a result of spanwise-heterogeneous ground roughness (see e.g. Wang & Cheng 2005; Fishpool, Lardeau & Leschziner 2009; Vermaas, Uijttewaal & Hoitink 2011), and they manifest as streamwise-elongated counter-rotating vortices that extend from the ground to the top of the boundary layer (Willingham *et al.* 2014; Anderson *et al.* 2015; Vanderwel & Ganapathisubramani 2015). Although our roughness is nominally homogeneous, the secondary flows in our LES are similar to the ones above spanwise-heterogeneous roughness.

Figures 7 and 8 show the streamwise velocity contours on a spanwise–wall-normal plane. The streamwise velocity is averaged both in time and in the streamwise direction. For brevity, we show results for three representative surface coverage densities, i.e. $\lambda_p = 0.08\,\%$, $1.0\,\%$ and $4.4\,\%$. The overlying vectors show the in-plane motions. The spanwise velocity and the wall-normal velocity are also averaged in time and in the streamwise direction. We see secondary flows. A pair of counter-rotating vortices is found on the two sides of a wall-mounted cube. For a given surface coverage density, there are twice as many windward projected cubes in staggered cases than in aligned cases; as a result, there are twice as many vortex pairs in staggered cases than in aligned cases. The counter-rotating vortices extend from the ground to the top of the boundary layer in A/S008 and A/S100, i.e. for cubes that are sparsely packed. At cube locations, the counter-rotating vortices bring high-speed

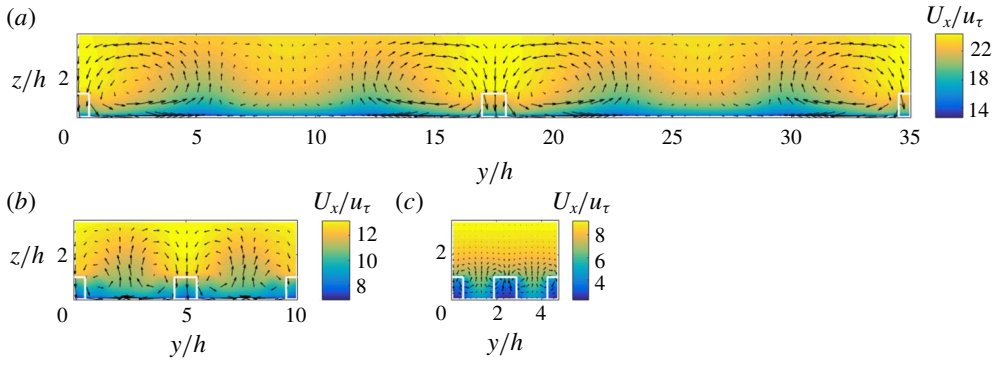

FIGURE 8. (Colour online) Same as figure 7, but for staggered cases (*a*) S008, (*b*) S100 and (*c*) S440.

fluid from the upper part of the boundary layer to the lower part, and on the two sides of the cubes, low-speed fluid in the lower part of the boundary layer is brought to the upper part. This leads to the spanwise heterogeneity in the streamwise velocity in figures 7 and 8, featuring high-speed flows above the cubes and low-speed flows on the two sides of the cubes. Because of the spanwise heterogeneity, U_h is an underestimate of the velocity of the incoming flows to the cubes, leading to a drag coefficient C_d that is $C_d > C_R$.

The wall-normal extents of the counter-rotating vortices decrease as the inter-cube distance decreases (see figures 7*c* and 8*c*). For A/S440, the outer flows are nearly homogeneous. Reynolds *et al.* (2007) found spanwise heterogeneity in the streamwise velocity above cube arrays of a surface coverage density $\lambda_p = 25\,\%$. Different from the secondary flows in figures 7 and 8, whose spanwise extents are confined by two columns of cubes, the high/low-momentum pathways in Reynolds *et al.* (2007) span approximately $4h$ in the spanwise direction and cover approximately two columns of cubes. As a result, the flow experiences a larger drag force at some cube locations than at others on average. This violates ergodicity. Considering that the secondary flows above spanwise-heterogeneous roughness and the secondary flows in our LES do not violate ergodicity, we think the secondary flows reported in Reynolds *et al.* (2007) are probably different flow features than the ones considered here.

Next, we briefly discuss how we may go about modelling the drag coefficient at low coverage densities. Figure 9 shows a sketch of the trailing vortices and the counter-rotating vortices (secondary flows). The trailing vortices join the counter-rotating vortices and strengthen them. We define s_x to be the streamwise inter-cube distance. (Per figure 3, for the aligned arrangement, $s_x = l = h/\sqrt{\lambda_p}$; and for the staggered arrangement, $s_x = 2l = 2h/\sqrt{\lambda_p}$.) If we fix s_x, the strength of the counter-rotating vortices is a function of s_y/L_z only, where s_y is the spanwise distance between two pairs of counter-rotating vortices, and L_z is the half-channel height (Anderson *et al.* 2018; Yang & Anderson 2018). It follows that, given s_x, then $C_d - C_R$ is a function of s_y/L_z only. A possible ansatz is

$$C_d/C_R - 1 = (s_y/L_z)^{-\alpha} g(s_x/h), \tag{3.1}$$

where g is a generic function and $\alpha > 0$ is a model parameter. Figure 10 shows $(C_d/C_R - 1)(s_y/L_z)^\alpha$ for $\alpha = 0.4$. The data collapse. For large s_x values, the cubes

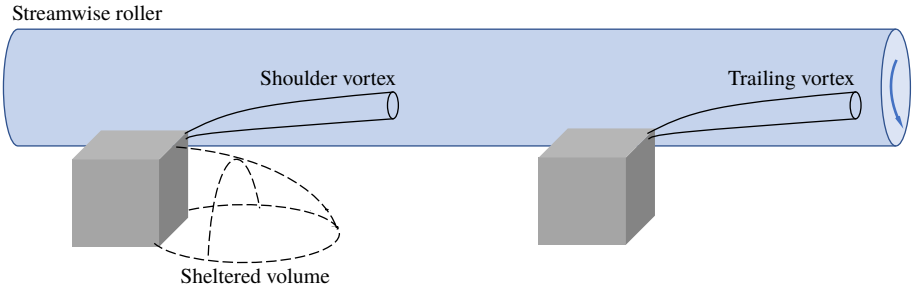

FIGURE 9. (Colour online) A sketch of the relevant flow structures. Flow is from left to right. For clarity, we have sketched flow structures on only one side of the cubes.

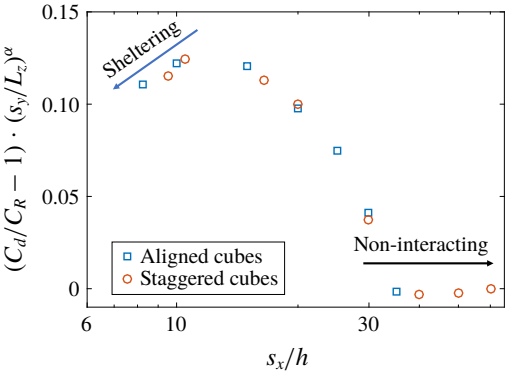

FIGURE 10. (Colour online) Plot of $(C_d/C_R - 1)(s_y/L_z)^\alpha$ as a function of s_x/h; $\alpha = 0.4$ is a parameter.

are non-interacting and $C_d = C_R$. For small s_x values, flow sheltering dominates, and C_d decreases as s_x decreases (as λ_p increases). For $10 < s_x/h < 35$, $C_d - C_R$ increases as s_x decreases, and $C_d/C_R - 1 = (s_y/L_z)^{-\alpha} g(s_x/h)$.

Next, we take a brief look at the friction on the ground. Compared with the drag forces on cubes, the friction on the ground is often small at high Reynolds numbers and is not the focus of this work. The near-wall turbulence is modelled instead of resolved in our LES; hence the wall shear stresses in our LES are less reliable (Yang, Bose & Moin 2017*a*). To study the wall shear stresses, we use DNS A100-d. The DNS computes flow in a half-channel above an array of aligned cubes with a surface coverage density of 1 %. Figure 11(*a*) shows the mean streamwise friction on the ground. Recirculation behind each wall-mounted cube leads to a region of reduced skin friction underneath the near wake, as expected. Underneath the far wake, we see two bands of high-stress regions. This is not expected from the classic drag partition theory, but is consistent with figure 9 and is responsible for the increase of the friction coefficient as a function of the surface coverage density. To the best of our knowledge, this is the first time a high-stress region has been found downstream of a cubical roughness.

To briefly summarize: we find secondary flows on homogeneously placed cubical roughness elements; the secondary flows manifest as counter-rotating vortices; as a result of the secondary flows, the spatially and temporally averaged wind speed at

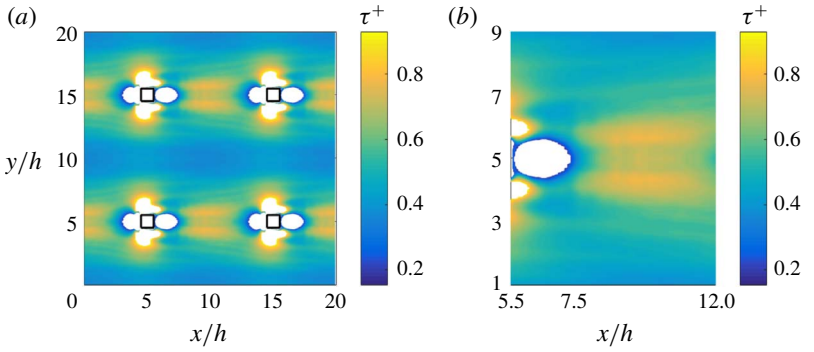

FIGURE 11. (Colour online) (*a*) Contours of the temporally averaged streamwise skin friction in case A100-d. (*b*) A zoomed view of the region underneath the far wake.

the cube height underestimates the velocity of the incoming flow to the cubes, and is more so when the secondary flows become stronger; as a result, the drag coefficient C_d takes values $C_d > C_R$. Detailed analysis shows that, for aligned and staggered cube arrays, the increase in the drag coefficient scales as $C_d/C_R - 1 = g(s_x/h)(s_y/L_z)^{-\alpha}$.

4. Further discussion on secondary flows

Turbulent secondary flows in rough-wall boundary layers have received a lot of attention in the recent literature. They are found above spanwise-heterogeneous roughness (see e.g. Mejia-Alvarez & Christensen 2013; Barros & Christensen 2014) and spanwise-heterogeneous superhydrophobic surfaces (Jelly, Jung & Zaki 2014; Lee, Jelly & Zaki 2015). Spanwise heterogeneity is often imposed by placing streamwise strips of closely packed roughness elements (see e.g. Nugroho, Hutchins & Monty 2013; Anderson *et al.* 2015; Vanderwel & Ganapathisubramani 2015; Yang & Anderson 2018), and the spanwise-heterogeneous surface roughness changes the flow dynamics in the outer layer. High-momentum pathways (HMPs) form above roughness strips, and low-momentum pathways (LMPs) form between two strips (Mejia-Alvarez & Christensen 2010). The nomenclature, i.e. HMPs and LMPs, is meant to distinguish the secondary flows from the high-speed and low-speed regions, which are transient in nature (see the detailed discussions in Meinhart & Adrian (1995), Hutchins & Marusic (2007) and de Silva, Hutchins & Marusic (2016)). Although the surface roughness in this work is nominally homogeneous, the secondary flows in our LES are very similar to the ones above spanwise-heterogeneous roughness. Figures 12 and 13 show the time-averaged streamwise velocity on a streamwise–spanwise plane at a distance $3h$ from the wall. Except for S440 (in figure 13*c*), LMPs and HMPs are found in all the cases. HMPs are found at cube locations, and LMPs are found on the sides of the cube locations. The HMPs and the LMPs are slightly compressed in the spanwise direction at locations downstream of the cubes, leading to weak streamwise heterogeneity. It is worth noting that the HMPs and LMPs could not be identified in instantaneous flow fields (see figures 14 and 15, where we show the contours of the instantaneous streamwise velocities on a spanwise–wall-normal plane at an equal distance from two rows of roughness elements).

The sizes of the secondary flows are confined by both the wall-mounted cubes and the half-channel height. At a relatively high surface coverage density, e.g. A440,

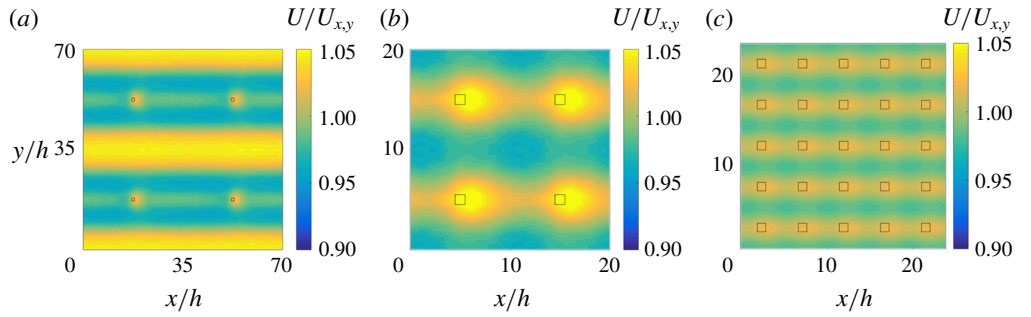

FIGURE 12. (Colour online) Contours of the time-averaged streamwise velocity on a streamwise–spanwise plane located at a distance $3h$ from the wall for aligned cases (*a*) A008, (*b*) A100 and (*c*) A440. The contour levels are kept the same among the plots.

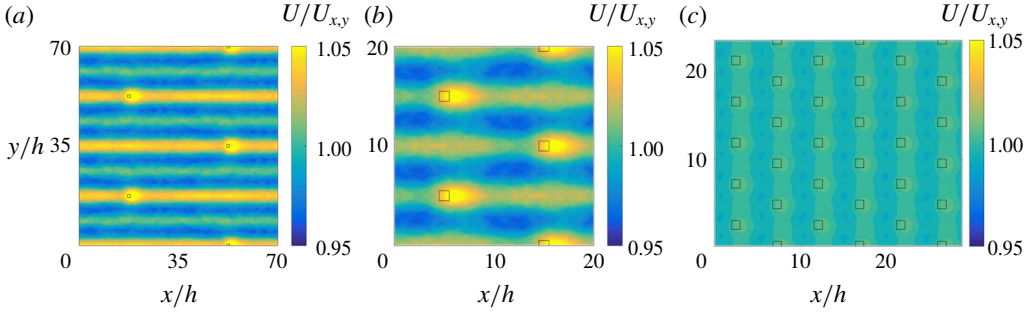

FIGURE 13. (Colour online) Same as figure 12, but for staggered cases (*a*) S008, (*b*) S100 and (*c*) S440.

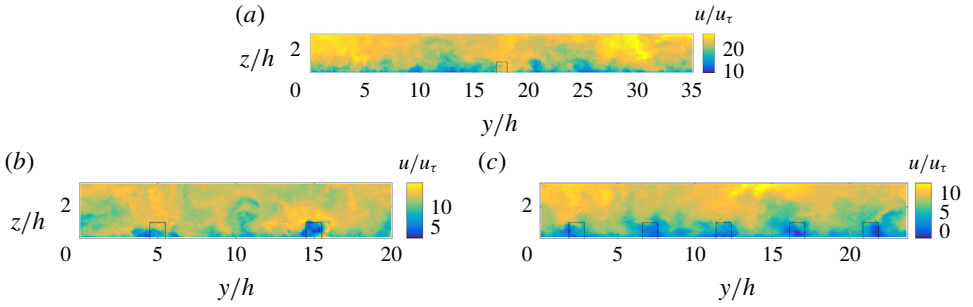

FIGURE 14. (Colour online) Contours of the instantaneous streamwise velocity on a spanwise–wall-normal plane located at an equal distance from two rows of cubes for aligned cases (*a*) A008, (*b*) A100 and (*c*) A440. The spanwise extent of the computational domain is 70. For a better presentation, we show only half of the computational domain.

the cubes dictate the sizes of the secondary flows; and at a low surface coverage density, e.g. A008, the half-channel height dictates the sizes of the secondary flows. Comparing A100, where the computational domain size is $L_x \times L_y \times L_z = 20h \times 20h \times 3.5h$, A100-w, where the computational domain size is $L_x \times L_y \times L_z = 40h \times 40h \times 3.5h$, and A100-h, where the computational domain size is $L_x \times L_y \times L_z = 40h \times 40h \times 7h$, we study the effect of the domain size at a somewhat intermediate surface coverage density. Figure 16(*a*) shows the streamwise- and time-averaged longitudinal velocity

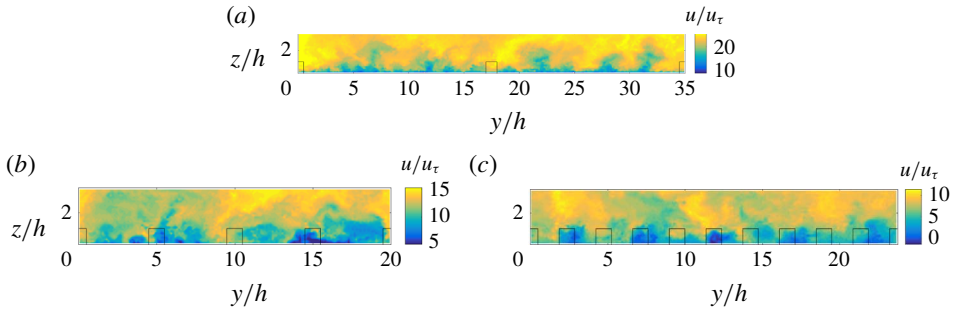

FIGURE 15. (Colour online) Same as figure 14, but for staggered cases (*a*) S008, (*b*) S100 and (*c*) S440.

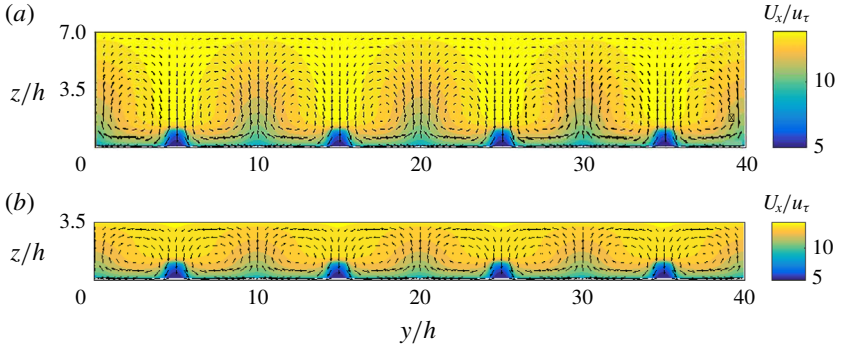

FIGURE 16. (Colour online) Contours of the streamwise- and time-averaged longitudinal velocity of (*a*) A100-h and (*b*) A100-w. The arrows show the in-plane motion.

of A100-h. Comparing with figures 7(*a*) and 16(*a*), the centres of the secondary vortices are at the same wall-normal locations. In the absence of secondary flows, a roughness sublayer, which is usually $3h$ to $5h$ (Lee *et al.* 2011), can be defined, and the flow is statistically homogeneous above the roughness sublayer. For A100-h, because the secondary vortices span the whole channel, the flow is nowhere statistically homogeneous. The measured drag coefficient is $C_d = 0.52$ from A100-h, which agrees reasonably well with that measured from A100, i.e. $C_d = 0.53$. Figure 16(*b*) shows the streamwise- and time-averaged longitudinal velocity of A100-w. Comparing A100 and A100-w, extending the computational domain in the streamwise and the spanwise directions does not seem to make any difference. The drag coefficient is $C_d = 0.53$ from A100-w, and is exactly the same as that measured from A100. Last, figure 17 shows the mean velocity profiles of A100, A100-h and A100-w. The three profiles agree reasonably well. This is particularly the case for the flow in the roughness layer.

So far, we have considered flows that are fully developed, for which a periodic boundary condition is imposed in the streamwise direction. Next, we consider flows that are developing, where the inflow is provided by a precursor channel flow simulation. We examine if secondary flows form shortly downstream and if the drag forces increase as a result. The two cases we will consider are A100-d and A440-d. Their fully developed counterparts, i.e. A100 and A440, show strong and weak secondary flow effects, respectively. Figure 18(*a*) shows the time-averaged streamwise velocity at a wall-normal distance $z = 1.2h$. A few rows downstream from the inlet,

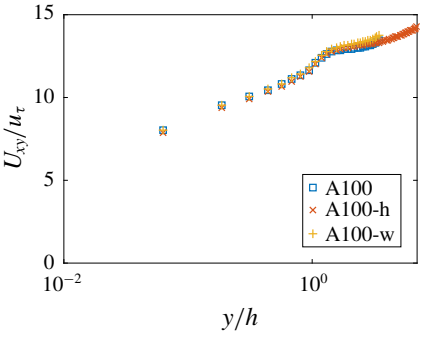

FIGURE 17. (Colour online) Mean velocity profiles of A100, A100-h and A100-w. Here U_{xy} is the streamwise-, spanwise- and time-averaged velocity.

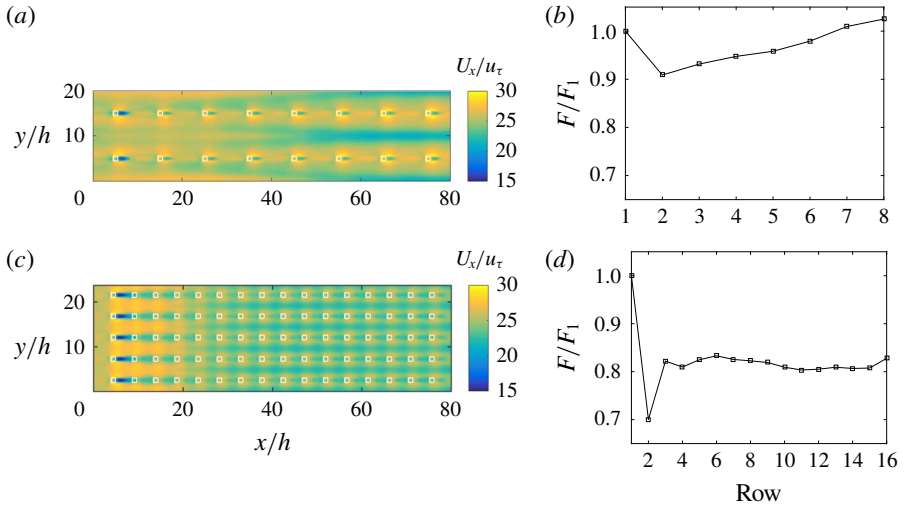

FIGURE 18. (Colour online) (*a*) Contours of time-averaged streamwise velocity at a wall-normal height $z = 1.2h$ in case A100-d. The wall area near the outlet is not mounted with cubes and is not shown. The cube locations are indicated with thin solid lines. (*b*) Normalized drag forces at each row for case A100-d. (*c*) Same as panel (*a*) but for A440-d. (*d*) Same as panel (*b*) but for A440-d.

HMPs form above the wall-mounted cubes and LMPs form in between. This is also clear from figure 19(*a*,*c*,*e*), where we show contours of the time-averaged streamwise velocity at various streamwise locations. Figure 18(*b*) shows the normalized drag force at each row. After a decrease in the normalized drag from the first row to the second due to flow sheltering (where the secondary vortices have not emerged yet), the drag force gradually increases as a result of secondary vortices, and at row 8, the drag is already above that of the first row. The results of A440-d are shown in figures 18(*c*,*d*), and 19(*b*,*d*,*f*). The flow field is much less heterogeneous in the spanwise direction, and the normalized drag increases only slightly from row 2 to row 17. Hence, it is probably safe to say that the secondary vortices we see in figures 7 and 8 are not artifacts of the periodic boundary condition.

Having verified that the secondary vortices in our LES are not artifacts of periodic boundary conditions nor a confined computational domain, we take a closer look

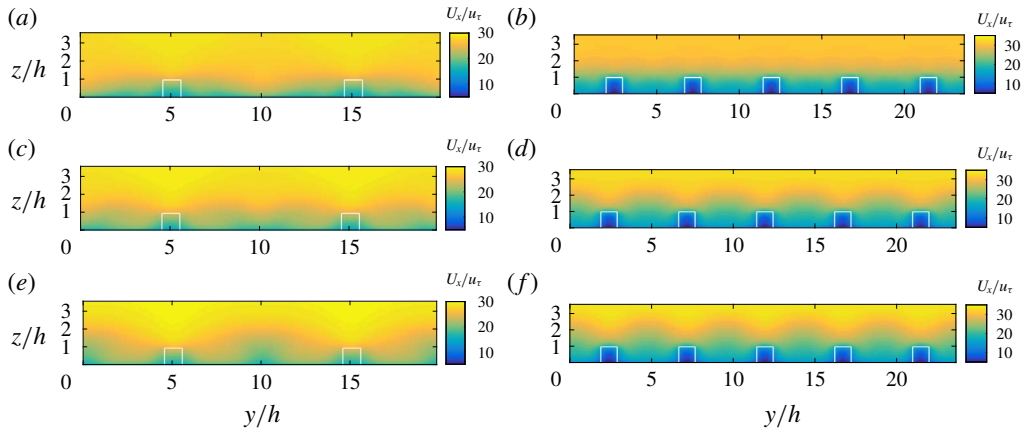

FIGURE 19. (Colour online) (*a*,*c*,*e*) Time-averaged streamwise velocity at $x = 20h$, $x = 40h$ and $x = 60h$, respectively, from A100-d. (*b*,*d*,*f*) Time-averaged streamwise velocity at $x = 21h$, $x = 40h$ and $x = 59h$, respectively, from A440-d. The streamwise locations are such that they are at the midpoint of two rows of roughness elements.

at these flow structures. A defining feature of secondary flows is that they carry a momentum flux. This could potentially pose a challenge to drag-force modelling. Although Raupach (1992) made no assumption about the mean flow, neglecting dispersive stresses in the Reynolds-averaged streamwise momentum equation is a common practice for rough-wall drag-force modelling (Macdonald 2000; Coceal & Belcher 2004; Harman & Finnigan 2007).

Here we derive the equation used in rough-wall modelling. The streamwise momentum equation reads

$$\frac{\partial u}{\partial t} + u\frac{\partial u}{\partial x} + v\frac{\partial u}{\partial y} + w\frac{\partial u}{\partial z} = -\frac{1}{\rho}\frac{\partial p}{\partial x} + \nu\left(\frac{\partial^2 u}{\partial x^2} + \frac{\partial^2 u}{\partial y^2} + \frac{\partial^2 u}{\partial z^2}\right) - f, \tag{4.1}$$

where f represents the drag force. Averaging in time, equations (4.1) leads to

$$\begin{aligned} &U\frac{\partial U}{\partial x} + V\frac{\partial U}{\partial y} + W\frac{\partial U}{\partial z} \\ &\quad + \frac{\partial\langle(u-U)(u-U)\rangle}{\partial x} + \frac{\partial\langle(u-U)(v-V)\rangle}{\partial y} + \frac{\partial\langle(u-U)(w-W)\rangle}{\partial z} \\ &\quad = -\frac{1}{\rho}\frac{\mathrm{d}P}{\mathrm{d}x} + \nu\left(\frac{\partial^2 U}{\partial x^2} + \frac{\partial^2 U}{\partial y^2} + \frac{\partial^2 U}{\partial z^2}\right) - F, \end{aligned} \tag{4.2}$$

where F is the time average of f. For simplicity, let us consider a periodic computational domain with constant half-channel height. Averaging in both the streamwise and the spanwise directions, equations (4.2) leads to

$$\begin{aligned} &-\frac{1}{\rho}\frac{\mathrm{d}P}{\mathrm{d}x} + \nu\frac{\mathrm{d}^2 U_{xy}}{\mathrm{d}z^2} - F_{xy} \\ &\quad - \frac{\mathrm{d}\langle(U-U_{xy})(W-W_{xy})\rangle_{xy}}{\mathrm{d}z} - \frac{\mathrm{d}\langle(u-U)(w-W)\rangle_{xy}}{\mathrm{d}z} = 0, \end{aligned} \tag{4.3}$$

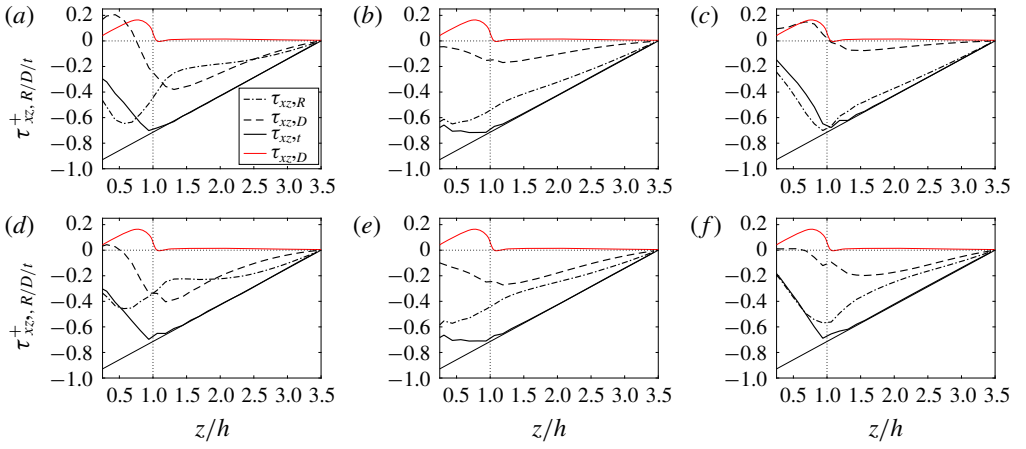

FIGURE 20. (Colour online) The Reynolds stresses, the dispersive stresses and the sum of the two for cases (*a*) A008, (*b*) A100, (*c*) A440, (*d*) S008, (*e*) S100 and (*f*) S440. The dot-dashed lines are the Reynolds stresses, the dashed lines are the dispersive stresses and the thick solid lines are the total stresses. The thin solid line corresponds to $\tau^+ = -1 + z/L_z$. The red line shows the dispersive stress in a rough-wall channel, where the roughness is staggered cubes of 25 % surface coverage density (Leonardi & Castro 2010).

where the first term represents a mean pressure force, the second term represents the viscous stress, the third term represents the drag force, the fourth term represents the dispersive stress and the fifth term represents the Reynolds stress. If one neglects dispersive stresses, the Reynolds-averaged streamwise momentum equation reads

$$-\frac{1}{\rho}\frac{\mathrm{d}P}{\mathrm{d}x} + \nu\frac{\mathrm{d}^2U_{xy}}{\mathrm{d}z^2} - \frac{\mathrm{d}\langle(u-U)(w-W)\rangle_{xy}}{\mathrm{d}z} - C_{ds}U_{xy}^2\frac{\mathrm{d}A_f(z)}{\mathrm{d}z} = 0, \tag{4.4}$$

where C_{ds} is the sectional drag coefficient and is often assumed to be constant, $A_f(z)$ is the frontal area under height z per unit planar area, and the subscript xy indicates streamwise and spanwise averaging. At high Reynolds numbers and in the absence of a streamwise pressure gradient, equation (4.4) reduces to

$$-\frac{\mathrm{d}\langle(u-U)(w-W)\rangle_{xy}}{\mathrm{d}z} - C_{ds}U_{xy}^2\frac{\mathrm{d}A_f(z)}{\mathrm{d}z} = 0, \tag{4.5}$$

which is often the starting point of rough-wall drag-force modelling.

Dispersive stresses are neglected in (4.5). Although dispersive stresses are not negligible in the roughness layer (Lien & Yee 2004; Martilli & Santiago 2007; Barlow & Coceal 2008), their effects can be modelled and absorbed in the drag coefficient C_{ds}; and therefore neglecting dispersive stresses is usually not problematic for drag-force modelling.

This is not the case for sparsely mounted cubes. Figure 20 shows the Reynolds stress $\tau_{xz,R} = \langle(u-U)(w-W)\rangle_{xy}$, the dispersive stress $\tau_{xz,R} = \langle UW\rangle_{xy} - U_{xy}W_{xy}$ and the 'total' stress $\tau_{xz,t} = \tau_{xz,R} + \tau_{xz,D}$ for cases A/S008, A/S100 and A/S440. Here, the subscript xz in τ_{xz} denotes the tensor direction, and the subscript xy in U_{xy} and W_{xy} denotes streamwise and spanwise averaging. The 'total' stress does not contain the subgrid stress nor the viscous stress. Subgrid stresses should be small if the flow is well resolved. Viscous stresses should be small if the flow is

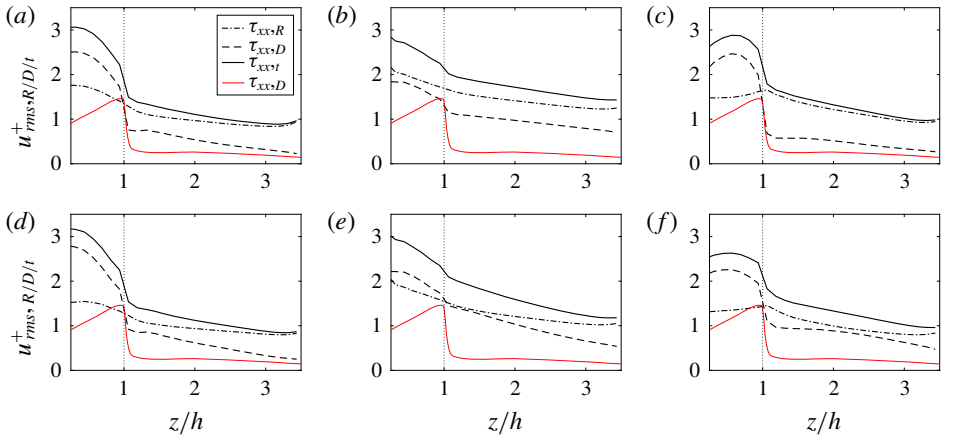

FIGURE 21. (Colour online) Same as figure 20, but for the streamwise component.

at high Reynolds numbers. Figure 20 shows the stresses above $z/h = 0.25$. The numerical solutions are less susceptible to numerical errors away from the wall (Kawai & Larsson 2012; Larsson *et al.* 2016). We make a few observations. First, the dispersive stress is practically zero at a coverage density $\lambda_p = 25\,\%$, and therefore it is not responsible for momentum transfer. Second, the total stresses in our LES follow $\tau^+ = -1 + z/L_z$ closely above $z/h = 1$ in all cases, and therefore the energy-containing scales in flows are 'well resolved' above the cube crest and the simulations are well converged. Third, the dispersive stresses in our LES are comparable with the Reynolds stresses. For cases A/S008, the dispersive stresses are responsible for more than half of the momentum fluxes at a distance approximately h above the cubes. For cases A/S100 and A/S440, the Reynolds stresses are the dominant component but the dispersive stresses are not negligible. If one includes the dispersive stress, the streamwise momentum equation is

$$-\frac{\mathrm{d}\langle(u-U)(w-W)\rangle_{xy}}{\mathrm{d}z} - \frac{\mathrm{d}(\langle UW\rangle_{xy} - U_{xy}W_{xy})}{\mathrm{d}z} - C_{ds}U_{xy}^2\frac{\mathrm{d}A_f(z)}{\mathrm{d}z} = 0, \tag{4.6}$$

where we have neglected the viscous and the pressure forces.

In (4.6), both the dispersive stress and the Reynolds stress need be modelled. To model the Reynolds stress, one could resort to an eddy viscosity model, and $-\tau_{R,xz} = \nu_T\,\mathrm{d}U/\mathrm{d}z$. As $-\tau_{R,xz}$ is positive definite, the eddy viscosity is also positive definite and therefore well defined. An eddy viscosity model is not possible for the dispersive stress, because it is not a positive definite quantity (see figure 20*a*), and one has to take a different approach. A similarity solution was recently proposed in Anderson *et al.* (2018). The similarity solution models the flow above the roughness and may be useful for modelling the dispersive stress, although, in its present form, the similarity solution assumes streamwise homogeneity and will have to be adapted for the flows considered in this work. In addition to the xz component of the dispersive stress, the xx component quantifies spanwise heterogeneity as well. Figure 21 shows the root-mean-square (r.m.s.) of the streamwise component of the dispersive stress tensor $\tau_{xx,D}$ as a function of the wall-normal distance; $\tau_{xx,D}$ is not negligible above sparsely packed cubes but is small if the cubes are packed closely ($\lambda_p = 25\,\%$).

The dispersive stress (the xz component) shows up in the x-momentum equation and therefore affects the mean flow scaling. Figure 22 shows the mean velocity profiles

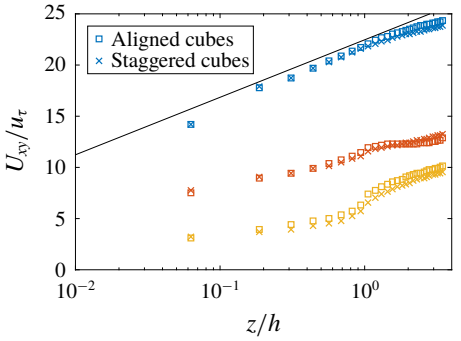

FIGURE 22. (Colour online) Mean velocity profiles. Squares are used for aligned cubes. Crosses are used for staggered cubes. Cases A/S008 are shown in blue. Cases A/S100 are shown in red. Cases A/S440 are shown in yellow. The thin solid line corresponds to the expected mean flow when there are no wall-mounted cubes, i.e. $U^+ = 1/\kappa \log(z/z_o)$.

in cases A/S008, A/S100 and A/S440. For cases A/S008, the cubes are very sparsely packed and the mean flow is not very different from that of a flat plate. The mean flows in cases A/S440 show typical behaviours as in rough-wall boundary layers (see e.g. Raupach *et al.* 1991; Squire *et al.* 2016). While the secondary flows do not affect much the mean flows in A/S440 and A/S008, the mean flows in A/S100 are noticeably modified by the secondary flows. Owing to the secondary-flow-induced mixing, the mean velocity profile is nearly flat above $z/h = 1$ in A100.

5. Concluding remarks

We conduct LES and DNS of flow in a half-channel with aligned and staggered cubes at the bottom wall. We study the properties of cube-roughened surfaces with a coverage density between $\lambda_p = 0.08\,\%$ and $\lambda_p = 4.4\,\%$. Although flow over cube arrays is a well-studied model problem for rough-wall turbulent boundary layers, there have not been many studies on rough walls with such a low coverage density ($\lambda_p < 1\,\%$).

Our findings are summarized below.

(i) For both aligned and staggered arrangements, we see an increase of the drag coefficient C_d and the friction coefficient C_f as a function of λ_p at low surface coverage densities. Since the seminal work by Raupach (1992), rough-wall drag-force modelling has been predominantly focusing on modelling the effects of flow sheltering, which only leads to a reduced drag coefficient and friction coefficient. Hence, the findings here pose a challenge to rough-wall drag-force modelling.

(ii) The observed increases in both C_d and C_f are the result of secondary turbulent flows. The secondary flows lead to HMPs at cube locations, which increases the incoming wind speed to wall-mounted cubes, and in turn leads to an increase in the drag coefficient. Visually, the secondary flows manifest as streamwise-elongated counter-rotating vortices in the mean flow fields. These secondary vortices are different from the commonly observed turbulent streaks, which are transient in nature (in time or in space).

(iii) The amount of increase in the drag coefficient is determined by the strength of the counter-rotating vortices and the distance between two neighbouring pairs of counter-rotating vortices, which may be parametrized with s_x/h and s_y/L_z, respectively. Detailed analysis shows that $(C_d/C_R - 1)(s_y/L_z)^\alpha$ collapses as a

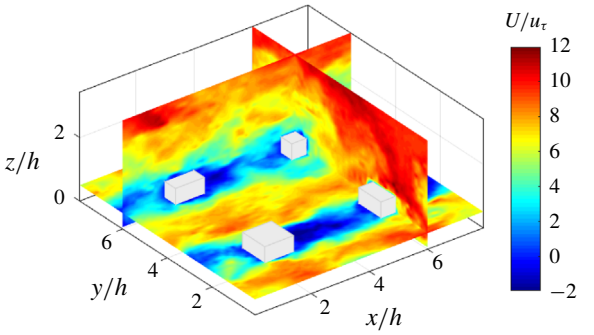

FIGURE 23. (Colour online) Contours of the instantaneous streamwise velocity on an x–y plane at a distance $0.5h$ from the wall, a y–z plane through the centre of a column of cubes, and an x–z plane through the centre of a row of cubes.

function of s_x/h for both aligned and staggered cube arrays, thereby providing a possible approach to drag-force modelling at low surface coverage densities.

(iv) The counter-rotating vortices enhance mixing and carry a significant part of the wall-normal momentum flux, leading to a non-negligible dispersive stress $\langle UW\rangle_{xy} - U_{xy}W_{xy}$. This poses yet another challenge to rough-wall drag-force modelling, as the common practice is to neglect the dispersive stress in the momentum balance.

(v) We also found two streamwise bands of high-stress regions beneath the far wake of a wall-mounted cube. As wakes have velocity deficits, the above finding is rather counter-intuitive.

The problem of flow over cube-roughened surfaces at low coverage densities can be approached from many perspectives. We have approached this problem from the perspective of drag-force modelling, and we have focused predominantly on first-order flow quantities. Rough surfaces with low coverage densities is still an under-explored area; we hope that this work will provide some preliminary yet useful information about the flow in that regime.

Acknowledgements

The computations are performed on the Penn State ACI. M.-W.G. acknowledges the National Natural Science Foundation of China (no. 11772128), the Fundamental Research Funds for the Central Universities (no. 2018ZD09) and the Scholarship from China Scholarship Council. We also wish to thank the three anonymous reviewers for their constructive comments and for their help in strengthening the paper.

Appendix A. A validation case against experiment

To validate our code, we conduct LES of flow in a half-channel with an array of aligned cubes at the bottom wall. The domain size is $8h \times 8h \times 3.5h$, where h is the height of the cubes. The surface coverage density is 6.25 %. We use the same resolution as the cases in table 1, and the mesh size is $64 \times 64 \times 28$. This corresponds to eight grid points across each direction of the cube. The boundary conditions are the same as those for the cases in table 1. Graham & Meneveau (2012) used the same setting for this flow. Figure 23 shows contours of the instantaneous streamwise velocity. We see low-speed regions behind the cubes and high-speed regions in

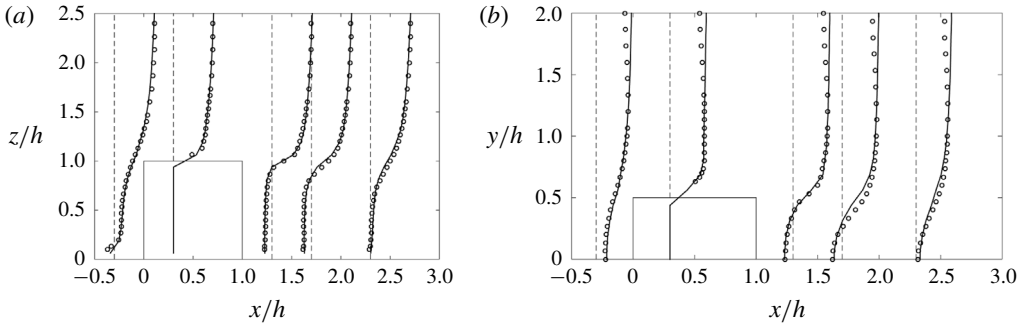

FIGURE 24. Mean velocity profiles compared with the experimental data at a few different streamwise locations: (*a*) an *x*–*z* plane through the centre of a column of cubes; and (*b*) an *x*–*y* plane at a distance $z = 0.5h$ from the wall. The solid lines are LESGO data, the dots are experimental results from Meinders & Hanjalić (1999) and the dashed lines indicate the measurement locations.

Name	λ_p (%)	Re_τ	$L_x \times L_y \times L_z$	Mesh	Mesh_h	N
A008-wrc	0.081	5.4×10^3	$70 \times 70 \times 3.5$	7.5M	36	2×2
A008-wrf	0.081	5.4×10^3	$70 \times 70 \times 3.5$	26M	52	2×2
A440-wrc	4.4	5.4×10^3	$24 \times 14 \times 3.5$	14M	30	5×3
A440-wrf	4.4	5.4×10^3	$24 \times 14 \times 3.5$	40M	50	5×3

TABLE 2. Details of the WRLES. The domain size is shown in terms of the cube height *h*. The 'Mesh' column shows the grid size in million (M) cells. The 'Mesh_h' column shows the number of grid points used to resolve one cube height. The column 'N' shows the number of wall-mounted cubes in columns (streamwise) and rows (spanwise). Again, we keep two significant digits.

between the cubes. In figure 24, we compare the LES results with the experimental measurements by Meinders & Hanjalić (1999) at a few streamwise locations. The LES results follow the experimental measurements closely. This work studies low-order statistics and therefore the present resolution suffices.

Appendix B. Validation against wall-resolved LES

To further validate our results, we conduct wall-resolved large-eddy simulation (WRLES) and compare WRLES with wall-modelled large-eddy simulation (WMLES). Details of the WRLES are tabulated in table 2. The nomenclature of the WRLES is as follows: A[λ_p]-wr[c/f], where λ_p is the surface coverage density (008 corresponds to 0.081 %, 440 corresponds to 4.4 %), 'wr' is wall-resolved, and c/f is coarse/fine grid. We carry out a grid convergence study. Figure 25 shows the mesh around a wall-mounted cube in A008-wrc, A008-wrf, A440-wrc and A440-wrf, respectively. The grid is non-uniform. The mesh is stretched away from the wall. The near-wall resolution is DNS-like and is kept unchanged between a coarse-grid LES and a fine-grid LES. A fine-grid LES has more grid points in the bulk than a coarse-grid LES, and the refinement ratio is approximately 1.5. We use 36, 52, 30 and 50 grid points to resolve one cube height in A008-wrc, A008-wrf, A440-wrc and A440-wrf, respectively. A typical WRLES uses approximately 20 to 30 grid points to resolve the

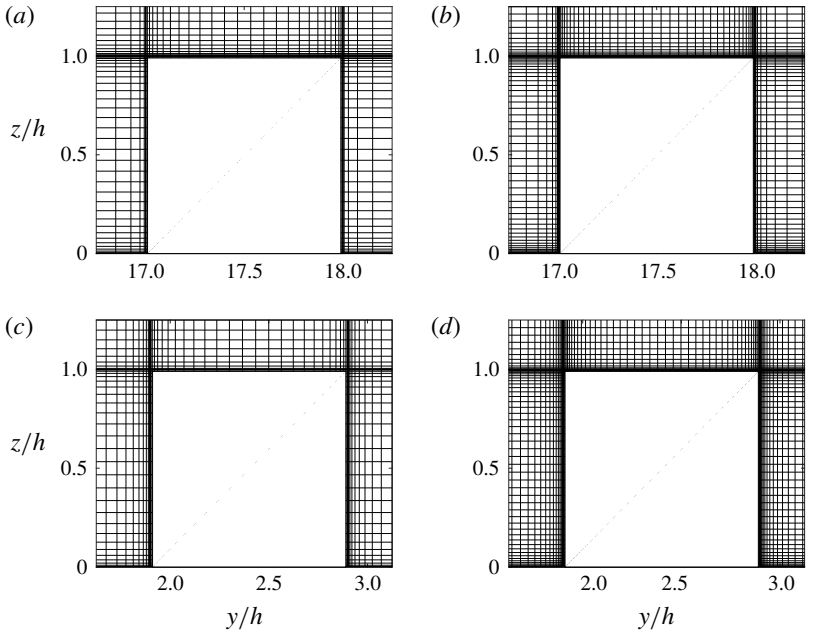

FIGURE 25. Grid around a wall-mounted cube in (*a*) A008-wrc, (*b*) A008-wrf, (*c*) A440-wrc and (*d*) A440-wrf.

bulk of the boundary layer Choi & Moin (2012). The coarse-grid LES, i.e. A008-wrc and A008-wrf, already comply with the above grid requirement. We use the in-house code CharLES for the WRLES calculations. The numerics of the code was already discussed in § 2.2. Here, the subgrid scales are modelled using the dynamic Vreman model (You & Moin 2007).

The counterparts of the WRLES are cases A008 and A440. The WMLES cases are at a nominally infinite Reynolds number, i.e. the viscosity is zero in the bulk of the flow. A viscous/roughness length scale z_o is imposed in the wall model. This length scale corresponds to $\nu/u_\tau \exp(-\kappa B)$, where κ is the von Kármán constant, and B is the addend in the logarithmic law of the wall. Hence the nominally infinite-Reynolds-number wall-modelled LES corresponds to a finite-Reynolds-number flow at $Re_\tau = L_z/z_o \exp(-\kappa B)$. In Stevens, Wilczek & Meneveau (2014), WMLES at nominally infinite Reynolds number are compared with finite-Reynolds-number wind tunnel experiments, and the statistics from the nominally infinite WMLES agrees well with that of the finite-Reynolds-number wind tunnel experiments up to the sixth order. The Reynolds number of our WRLES is determined following Stevens *et al.* (2014).

Table 3 compares the drag coefficient C_d in our WRLES and WMLES. The results match up to two significant digits; C_d is a zeroth-order statistic. Predicting C_d is usually not difficult. In fact, by prescribing the flow separation locations, one could predict the pressure drag and lift coefficients of an airfoil using an inviscid code, which does not resolve the wall layer nor the wake. In the present cases, flow separates at the trailing edge of the cube irrespective of the WRLES/WMLES used, and the leeward surface is immersed in the separated region. Thus, the pressure on the leeward surface does not depend critically on the WRLES/WMLES. This is probably why the WRLES and WMLES yield almost the same C_d despite the difference in the

Name	C_d	Name	C_d	Name	C_d
A008-wrc	0.49	A008-wrf	0.49	A008	0.49
A440-wrc	0.44	A440-wrf	0.44	A440	0.44

TABLE 3. Drag coefficients in WMLES and WRLES. Again, we have kept two significant digits.

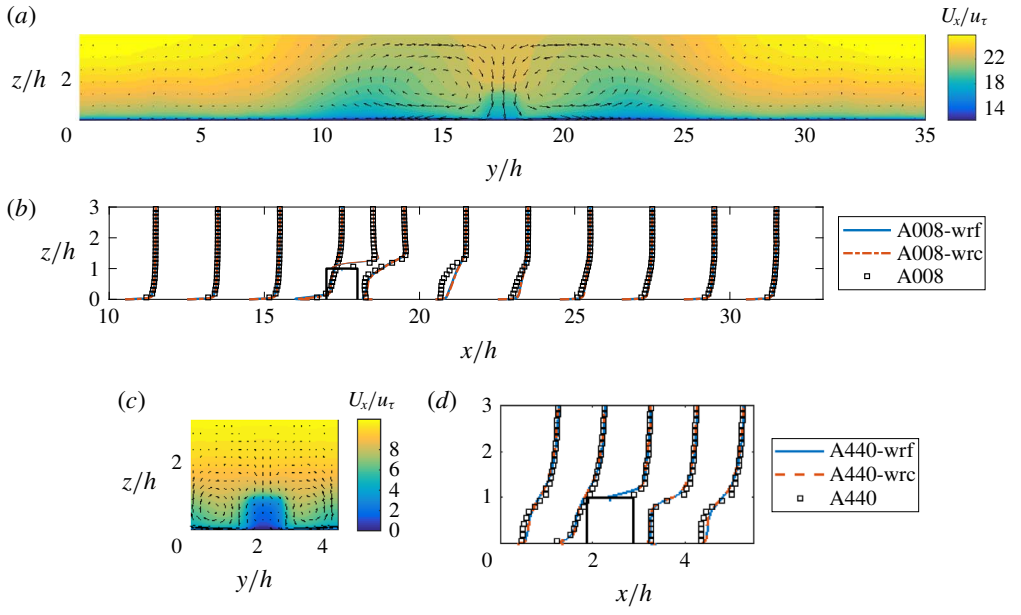

FIGURE 26. (Colour online) (*a*) Contours of the streamwise- and time-averaged longitudinal velocity in the case A008-wrc. The arrows show the in-plane motions. (*b*) A comparison of the time-mean streamwise velocity at a spanwise location through the centre of the cube and at various x locations. The cube location is indicated. The coarse-grid WRLES results are on top of the fine-grid WRLES results. (*c*) Same as panel (*a*) but for case A440-wrc. (*d*) Same as panel (*b*) but for surface coverage density 4.4 %.

velocity above the crest and further downstream (shown after). In the following, we take a look at the velocity, which is usually more difficult to predict than the drag coefficient.

Figure 26(*a*,*c*) shows the contours of the streamwise- and time-averaged longitudinal velocity in cases A008-wrf and A440-wrf. The results compare well with figure 7(*a*,*c*). In figure 26(*b*,*d*), we compare WMLES with WRLES at a spanwise location through the cube centre and at various streamwise locations. The WRLES calculations are grid-converged. A008-wrc is no different from A008-wrf, and A440-wrc is no different from A440-wrf. The WMLES results follow the WRLES results closely both upstream and immediately downstream of the cube. Differences are found in the wake and above the cube crest. Despite this difference, the drag coefficient in WRLES matches that in WMLES (in table 3). This is because the drag force on a wall-mounted cube depends on the pressure but not so much the skin friction.

In this paper, we have mainly looked at the behaviour of the drag force on the cubes. In the main part of the paper, we argued that, because the wall layer is modelled in

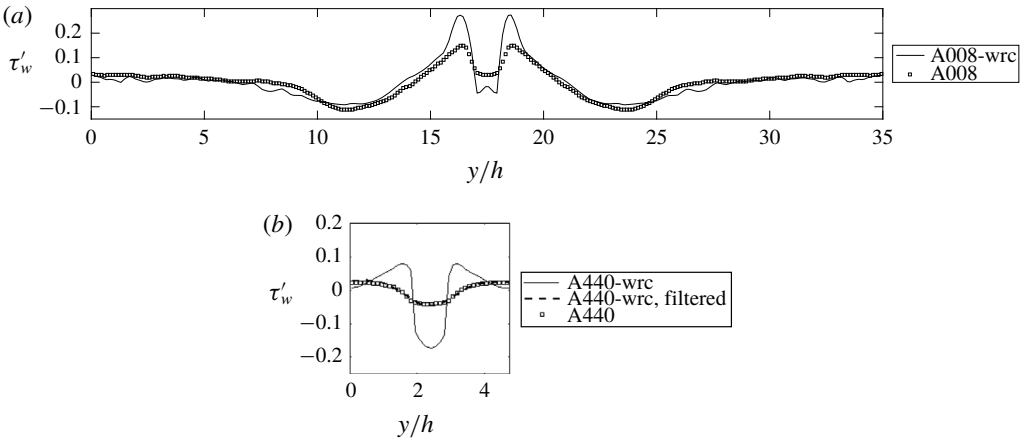

FIGURE 27. (*a*) The streamwise- and time-averaged skin friction in A008-wrc and A008. (*b*) The streamwise- and time-averaged skin friction in A440-wrc and A440. 'A440-wrc, filtered' is A440-wrc subjected to a Gaussian filtration.

a WMLES, the skin-friction prediction in a WMLES is not reliable. The skin friction C_f is shown only in figure 6(*b*). In that context, C_f is a derived quantity from the drag coefficient:

$$C_f = \frac{\tau_s}{\rho U_h^2} = \frac{-\dfrac{\mathrm{d}P}{\mathrm{d}x}L_z - \dfrac{f}{h^2}\lambda_p}{\rho U_h^2} = \frac{u_\tau^2}{U_h^2} - C_d\lambda_p. \tag{B 1}$$

However, it is of interest to take a look at how WMLES does for the skin friction. Considering that the secondary flows are streamwise-elongated structures, it is probably more informative to show the time-averaged and streamwise-averaged wall shear stress as a function of the spanwise coordinate. Figure 27 shows the streamwise- and time-averaged wall shear stress in A008-wrc, A008, A440-wrc and A440. The fine-grid WRLES results are not different from those for the coarse-grid WRLES and are not shown here for brevity. At $\lambda_p = 0.081\,\%$, the WMLES follows the WRLES in general, but because the wall layer is not resolved in WMLES, the WMLES misses the details that are present in the WRLES. The cube is located at $y/h = 17.5$. The footprints of both the HMPs and the LMPs are found: HMPs manifest as two peaks in the immediate vicinity of the cube, and LMPs manifest as two valleys further away from the cube location. At $\lambda_p = 4.4\,\%$, the WMLES results look smeared and do not agree well with the WRLES. An interesting observation is that the Gaussian filtered WRLES stress agrees well with the WMLES.

REFERENCES

AKINS, R. E., PETERKA, J. A. & CERMAK, J. E. 1977 Mean force and moment coefficients for buildings in turbulent boundary layers. *J. Wind Engng Ind. Aerodyn.* **2** (3), 195–209.

ANDERSON, W., BARROS, J. M., CHRISTENSEN, K. T. & AWASTHI, A. 2015 Numerical and experimental study of mechanisms responsible for turbulent secondary flows in boundary layer flows over spanwise heterogeneous roughness. *J. Fluid Mech.* **768**, 316–347.

ANDERSON, W., YANG, J., SHRESTHA, K. & AWASTHI, A. 2018 Turbulent secondary flows in wall turbulence: vortex forcing, scaling arguments, and similarity solution. *Environ. Fluid Mech.* **18** (6), 1351–1378.

ARYA, S. 1975 A drag partition theory for determining the large-scale roughness parameter and wind stress on the Arctic pack ice. *J. Geophys. Res.* **80** (24), 3447–3454.

BALAKUMAR, P., PARK, G. & PIERCE, B. 2014 DNS, LES, and wall-modeled LES of separating flow over periodic hills. In *Proceedings of the Summer Program*, pp. 407–415.

BARLOW, J. F. & COCEAL, O. 2009 A review of urban roughness sublayer turbulence. Met Office Research and Development. *Tech. Rep.* 1, 527.

BARROS, J. M. & CHRISTENSEN, K. T. 2014 Observations of turbulent secondary flows in a rough-wall boundary layer. *J. Fluid Mech.* **748**, R1.

BERMEJO-MORENO, I., CAMPO, L., LARSSON, J., BODART, J., HELMER, D. & EATON, J. K. 2014 Confinement effects in shock wave/turbulent boundary layer interactions through wall-modelled large-eddy simulations. *J. Fluid Mech.* **758**, 5–62.

BONS, J. P. 2010 A review of surface roughness effects in gas turbines. *Trans. ASME J. Turbomach.* **132** (2), 021004.

BOU-ZEID, E., MENEVEAU, C. & PARLANGE, M. 2005 A scale-dependent Lagrangian dynamic model for large eddy simulation of complex turbulent flows. *Phys. Fluids* **17** (2), 025105.

CASTILLO, M. C., INAGAKI, A. & KANDA, M. 2011 The effects of inner- and outer-layer turbulence in a convective boundary layer on the near-neutral inertial sublayer over an urban-like surface. *Boundary-Layer Meteorol.* **140** (3), 453–469.

CHENG, H. & CASTRO, I. P. 2002 Near wall flow over urban-like roughness. *Boundary-Layer Meteorol.* **104** (2), 229–259.

CHENG, H., HAYDEN, P., ROBINS, A. & CASTRO, I. 2007 Flow over cube arrays of different packing densities. *J. Wind Engng Ind. Aerodyn.* **95** (8), 715–740.

CHENG, W.-C. & PORTÉ-AGEL, F. 2015 Adjustment of turbulent boundary-layer flow to idealized urban surfaces: a large-eddy simulation study. *Boundary-Layer Meteorol.* **155** (2), 249–270.

CHOI, H. & MOIN, P. 2012 Grid-point requirements for large eddy simulation: Chapmans estimates revisited. *Phys. Fluids* **24** (1), 011702.

CHUNG, D., CHAN, L., MACDONALD, M., HUTCHINS, N. & OOI, A. 2015 A fast direct numerical simulation method for characterising hydraulic roughness. *J. Fluid Mech.* **773**, 418–431.

COCEAL, O. & BELCHER, S. 2004 A canopy model of mean winds through urban areas. *Q. J. R. Meteorol. Soc.* **130** (599), 1349–1372.

COCEAL, O., DOBRE, A. & THOMAS, T. G. 2007*a* Unsteady dynamics and organized structures from dns over an idealized building canopy. *Intl J. Climatol.* **27** (14), 1943–1953.

COCEAL, O., DOBRE, A., THOMAS, T. & BELCHER, S. 2007*b* Structure of turbulent flow over regular arrays of cubical roughness. *J. Fluid Mech.* **589**, 375–409.

COCEAL, O., THOMAS, T., CASTRO, I. & BELCHER, S. 2006 Mean flow and turbulence statistics over groups of urban-like cubical obstacles. *Boundary-Layer Meteorol.* **121** (3), 491–519.

ESDU 1986 Mean fluid forces and moments on rectangular prisms: surface-mounted structures in turbulent shear flow. *Engng Sci. Data Item* **8003**.

FERSTER, K. K., KIRSCH, K. L. & THOLE, K. A. 2018 Effects of geometry, spacing, and number of pin fins in additively manufactured microchannel pin fin arrays. *Trans. ASME J. Turbomach.* **140** (1), 011007.

FISHPOOL, G., LARDEAU, S. & LESCHZINER, M. 2009 Persistent non-homogeneous features in periodic channel-flow simulations. *Flow Turbul. Combust.* **83** (3), 323–342.

GIOMETTO, M., LOZANO-DURAN, A., PARK, G. & MOIN, P. 2017 Three-dimensional transient channel flow at moderate Reynolds numbers: analysis and wall modeling. In *Annual Research Briefs*, pp. 65–74. Center for Turbulence Research.

GRAHAM, J. & MENEVEAU, C. 2012 Modeling turbulent flow over fractal trees using renormalized numerical simulation: alternate formulations and numerical experiments. *Phys. Fluids* **24** (12), 125105.

HARMAN, I. N. & FINNIGAN, J. J. 2007 A simple unified theory for flow in the canopy and roughness sublayer. *Boundary-Layer Meteorol.* **123** (2), 339–363.

HUTCHINS, N. & MARUSIC, I. 2007 Evidence of very long meandering features in the logarithmic region of turbulent boundary layers. *J. Fluid Mech.* **579**, 1–28.

INAGAKI, A., CASTILLO, M. C. L., YAMASHITA, Y., KANDA, M. & TAKIMOTO, H. 2012 Large-eddy simulation of coherent flow structures within a cubical canopy. *Boundary-Layer Meteorol.* **142** (2), 207–222.

JELLY, T., JUNG, S. & ZAKI, T. 2014 Turbulence and skin friction modification in channel flow with streamwise-aligned superhydrophobic surface texture. *Phys. Fluids* **26** (9), 095102.

JIANG, D., JIANG, W., LIU, H. & SUN, J. 2008 Systematic influence of different building spacing, height and layout on mean wind and turbulent characteristics within and over urban building arrays. *Wind Struct.* **11** (4), 275–290.

JIMÉNEZ, J. 2004 Turbulent flows over rough walls. *Annu. Rev. Fluid Mech.* **36**, 173–196.

JOO, J., MEDIC, G., PHILIPS, D. & BOSE, S. 2014 Large-eddy simulation of a compressor rotor. In *Proceedings of the Summer Program*, p. 467.

VON KÁRMÁN, T. 1931 Mechanical similitude and turbulence, *NACA Tech. Memorandum, Rep. No.* 611.

KAWAI, S. & LARSSON, J. 2012 Wall-modeling in large eddy simulation: length scales, grid resolution, and accuracy. *Phys. Fluids* **24** (1), 015105.

KHALIGHI, Y., HAM, F., NICHOLS, J., LELE, S. & MOIN, P. 2011 Unstructured large eddy simulation for prediction of noise issued from turbulent jets in various configurations. In *17th AIAA/CEAS Aeroacoustics Conference (32nd AIAA Aeroacoustics Conference)*, p. 2886.

KIRSCH, K. L. & THOLE, K. A. 2018 Isolating the effects of surface roughness versus wall shape in numerically optimized, additively manufactured micro cooling channels. *Exp. Therm. Fluid Sci.* **98**, 227–238.

LARSSON, J., KAWAI, S., BODART, J. & BERMEJO-MORENO, I. 2016 Large eddy simulation with modeled wall-stress: recent progress and future directions. *Mech. Engng Rev.* **3** (1), 15–00418.

LARSSON, J., LAURENCE, S., BERMEJO-MORENO, I., BODART, J., KARL, S. & VICQUELIN, R. 2015 Incipient thermal choking and stable shock-train formation in the heat-release region of a scramjet combustor. Part II: large eddy simulations. *Combust. Flame* **162** (4), 907–920.

LEE, J., JELLY, T. O. & ZAKI, T. A. 2015 Effect of Reynolds number on turbulent drag reduction by superhydrophobic surface textures. *Flow Turbul. Combust.* **95** (2–3), 277–300.

LEE, J. H., SUNG, H. J. & KROGSTAD, P.-Å 2011 Direct numerical simulation of the turbulent boundary layer over a cube-roughened wall. *J. Fluid Mech.* **669**, 397–431.

LELE, S. K. 1994 Compressibility effects on turbulence. *Annu. Rev. Fluid Mech.* **26** (1), 211–254.

LEONARDI, S. & CASTRO, I. P. 2010 Channel flow over large cube roughness: a direct numerical simulation study. *J. Fluid Mech.* **651**, 519–539.

LIEN, F.-S. & YEE, E. 2004 Numerical modelling of the turbulent flow developing within and over a 3-D building array, Part I: a high-resolution Reynolds-averaged Navier–Stokes approach. *Boundary-Layer Meteorol.* **112** (3), 427–466.

LOZANO-DURÁN, A. & JIMÉNEZ, J. 2014 Effect of the computational domain on direct simulations of turbulent channels up to $Re_\tau = 4200$. *Phys. Fluids* **26** (1), 011702.

MACDONALD, R. 2000 Modelling the mean velocity profile in the urban canopy layer. *Boundary-Layer Meteorol.* **97** (1), 25–45.

MACDONALD, M., CHUNG, D., HUTCHINS, N., CHAN, L., OOI, A. & GARCÍA-MAYORAL, R. 2016 The minimal channel: a fast and direct method for characterising roughness. *J. Phys.: Conf. Ser.* **708**, 012010.

MACDONALD, M., CHUNG, D., HUTCHINS, N., CHAN, L., OOI, A. & GARCÍA-MAYORAL, R. 2017 The minimal-span channel for rough-wall turbulent flows. *J. Fluid Mech.* **816**, 5–42.

MACDONALD, R., GRIFFITHS, R. & HALL, D. 1998 An improved method for the estimation of surface roughness of obstacle arrays. *Atmos. Environ.* **32** (11), 1857–1864.

MAHESH, K., CONSTANTINESCU, G. & MOIN, P. 2004 A numerical method for large-eddy simulation in complex geometries. *J. Comput. Phys.* **197** (1), 215–240.

MARTILLI, A. & SANTIAGO, J. L. 2007 CFD simulation of airflow over a regular array of cubes. Part II: analysis of spatial average properties. *Boundary-Layer Meteorol.* **122** (3), 635–654.

MARUSIC, I., MONTY, J. P., HULTMARK, M. & SMITS, A. J. 2013 On the logarithmic region in wall turbulence. *J. Fluid Mech.* **716**, R3.

MEINDERS, E. & HANJALIĆ, K. 1999 Vortex structure and heat transfer in turbulent flow over a wall-mounted matrix of cubes. *Intl J. Heat Fluid Flow* **20** (3), 255–267.

MEINHART, C. D. & ADRIAN, R. J. 1995 On the existence of uniform momentum zones in a turbulent boundary layer. *Phys. Fluids* **7** (4), 694–696.

MEJIA-ALVAREZ, R. & CHRISTENSEN, K. 2010 Low-order representations of irregular surface roughness and their impact on a turbulent boundary layer. *Phys. Fluids* **22** (1), 015106.

MEJIA-ALVAREZ, R. & CHRISTENSEN, K. 2013 Wall-parallel stereo particle-image velocimetry measurements in the roughness sublayer of turbulent flow overlying highly irregular roughness. *Phys. Fluids* **25** (11), 115109.

MENEVEAU, C. & KATZ, J. 2000 Scale-invariance and turbulence models for large-eddy simulation. *Annu. Rev. Fluid Mech.* **32** (1), 1–32.

MILLWARD-HOPKINS, J., TOMLIN, A., MA, L., INGHAM, D. & POURKASHANIAN, M. 2011 Estimating aerodynamic parameters of urban-like surfaces with heterogeneous building heights. *Boundary-Layer Meteorol.* **141** (3), 443–465.

MOIN, P. 2010 *Fundamentals of Engineering Numerical Analysis*. Cambridge University Press.

MOODY, L. F. 1947 An approximate formula for pipe friction factors. *Trans. ASME* **69** (12), 1005–1011.

NAKAGAWA, H. 2017 *Turbulence in Open Channel Flows*. Routledge.

NIKURADSE, J. 1930 Investigation of turbulent flow in tubes of non-circular cross section. *Engng Archive (Ingen. Arch.)* **1**, 306–332.

NUGROHO, B., HUTCHINS, N. & MONTY, J. 2013 Large-scale spanwise periodicity in a turbulent boundary layer induced by highly ordered and directional surface roughness. *Intl J. Heat Fluid Flow* **41**, 90–102.

PARK, G. I. 2017 Wall-modeled large-eddy simulation of a high Reynolds number separating and reattaching flow. *AIAA J.* **55**, 3709–3721.

PARK, G. I. & MOIN, P. 2014 An improved dynamic non-equilibrium wall-model for large eddy simulation. *Phys. Fluids* **26** (1), 37–48.

PERRET, L., PIQUET, T., BASLEY, J. & MATHIS, R. 2017 Effects of plan area densities of cubical roughness elements on turbulent boundary layers. In *ScienceConf, CFM*.

PERRY, A. E., SCHOFIELD, W. H. & JOUBERT, P. N. 1969 Rough wall turbulent boundary layers. *J. Fluid Mech.* **37** (2), 383–413.

RAUPACH, M. 1992 Drag and drag partition on rough surfaces. *Boundary-Layer Meteorol.* **60** (4), 375–395.

RAUPACH, M., ANTONIA, R. & RAJAGOPALAN, S. 1991 Rough-wall turbulent boundary layers. *Appl. Mech. Rev.* **44** (1), 1–25.

REYNOLDS, R., HAYDEN, P., CASTRO, I. & ROBINS, A. 2007 Spanwise variations in nominally two-dimensional rough-wall boundary layers. *Exp. Fluids* **42** (2), 311–320.

SCHLICHTING, H. & GERSTEN, K. 2016 *Boundary-Layer Theory*. Springer.

SCHULTZ, M. P. & FLACK, K. A. 2009 Turbulent boundary layers on a systematically varied rough wall. *Phys. Fluids* **21** (1), 015104.

SHAO, Y. & YANG, Y. 2005 A scheme for drag partition over rough surfaces. *Atmos. Environ.* **39** (38), 7351–7361.

SHAO, Y. & YANG, Y. 2008 A theory for drag partition over rough surfaces. *J. Geophys. Res.* **113**, F02S05.

DE SILVA, C. M., HUTCHINS, N. & MARUSIC, I. 2016 Uniform momentum zones in turbulent boundary layers. *J. Fluid Mech.* **786**, 309–331.

SLOTNICK, J., KHODADOUST, A., ALONSO, J., DARMOFAL, D., GROPP, W., LURIE, E. & MAVRIPLIS, D. 2014 CFD vision 2030 study: a path to revolutionary computational aerosciences. *Technical Report, NASA Langley Research Center*, NASA/CR-2014-218178. See http://ntrs.nasa.gov/archive/nasa/casi.ntrs.nasa.gov/20140003093.pdf/.

SQUIRE, D., MORRILL-WINTER, C., HUTCHINS, N., SCHULTZ, M., KLEWICKI, J. & MARUSIC, I. 2016 Comparison of turbulent boundary layers over smooth and rough surfaces up to high Reynolds numbers. *J. Fluid Mech.* **795**, 210–240.

STEVENS, R. J., WILCZEK, M. & MENEVEAU, C. 2014 Large-eddy simulation study of the logarithmic law for second- and higher-order moments in turbulent wall-bounded flow. *J. Fluid Mech.* **757**, 888–907.

STOESSER, T., MATHEY, F., FROHLICH, J. & RODI, W. 2003 Les of flow over multiple cubes. *Ercoftac Bull.* **56**, 15–19.

TAYLOR, R., COLEMAN, H. & HODGE, B. 1985 Prediction of turbulent rough-wall skin friction using a discrete element approach. *Trans. ASME J. Fluids Engng* **107** (2), 251–257.

VANDERWEL, C. & GANAPATHISUBRAMANI, B. 2015 Effects of spanwise spacing on large-scale secondary flows in rough-wall turbulent boundary layers. *J. Fluid Mech.* **774**, R2.

VERMAAS, D., UIJTTEWAAL, W. & HOITINK, A. 2011 Lateral transfer of streamwise momentum caused by a roughness transition across a shallow channel. *Water Resour. Res.* **47**, W02530.

WANG, Z.-Q. & CHENG, N.-S. 2005 Secondary flows over artificial bed strips. *Adv. Water Resour.* **28** (5), 441–450.

WILLIAMSON, J. 1980 Low-storage Runge–Kutta schemes. *J. Comput. Phys.* **35** (1), 48–56.

WILLINGHAM, D., ANDERSON, W., CHRISTENSEN, K. T. & BARROS, J. M. 2014 Turbulent boundary layer flow over transverse aerodynamic roughness transitions: induced mixing and flow characterization. *Phys. Fluids* **26** (2), 025111.

XIE, Z. & CASTRO, I. P. 2006 Les and rans for turbulent flow over arrays of wall-mounted obstacles. *Flow Turbul. Combust.* **76** (3), 291–312.

YANG, X. I. A. 2016 On the mean flow behaviour in the presence of regional-scale surface roughness heterogeneity. *Boundary-Layer Meteorol.* **161** (1), 127–143.

YANG, X. I. A. & ABKAR, M. 2018 A hierarchical random additive model for passive scalars in wall-bounded flows at high Reynolds numbers. *J. Fluid Mech.* **842**, 354–380.

YANG, J. & ANDERSON, W. 2018 Numerical study of turbulent channel flow over surfaces with variable spanwise heterogeneities: topographically-driven secondary flows affect outer-layer similarity of turbulent length scales. *Flow Turbul. Combust.* **100** (1), 1–17.

YANG, X., BOSE, S. & MOIN, P. 2017*a* A physics-based interpretation of the slip-wall LES model. In *Annual Research Briefs*, pp. 65–74. Center for Turbulence Research.

YANG, X. I. A. & MENEVEAU, C. 2016 Large eddy simulations and parameterisation of roughness element orientation and flow direction effects in rough wall boundary layers. *J. Turbul.* **17** (11), 1072–1085.

YANG, X. I. A. & MENEVEAU, C. 2017 Modelling turbulent boundary layer flow over fractal-like multiscale terrain using large-eddy simulations and analytical tools. *Phil. Trans. R. Soc. Lond.* A **375** (2091), 20160098.

YANG, X. I. A., PARK, G. I. & MOIN, P. 2017*b* Log-layer mismatch and modeling of the fluctuating wall stress in wall-modeled large-eddy simulations. *Phys. Rev. Fluids* **2** (10), 104601.

YANG, X. I. A., SADIQUE, J., MITTAL, R. & MENEVEAU, C. 2016 Exponential roughness layer and analytical model for turbulent boundary layer flow over rectangular-prism roughness elements. *J. Fluid Mech.* **789**, 127–165.

YOU, D. & MOIN, P. 2007 A dynamic global-coefficient subgrid-scale eddy-viscosity model for large-eddy simulation in complex geometries. *Phys. Fluids* **19** (6), 065110.